

# Assessment of Arctic Sea Ice Thickness Retrieval Ability of the Chinese HY-2B Ku-band Radar Altimeter

Zhaoqing Dong<sup>1,2</sup>, Lijian Shi<sup>2,3</sup>, Mingsen Lin<sup>2,3</sup>, Yongjun Jia<sup>2,3</sup>, Tao Zeng<sup>2,3</sup>, Suhui Wu<sup>2</sup>

<sup>1</sup>Hohai University, Nanjing, 210003, China

5 <sup>2</sup>National Satellite Ocean Application Service, Beijing, 100081, China

<sup>3</sup>Key Laboratory of Space Ocean Remote Sensing and Application (MNR), Beijing, 100081, China

Correspondence to: Lijian Shi (shilj@mail.nsoas.org.cn)

**Abstract.** With the continuous development of the China Ocean Dynamic Environment Satellite Series (Haiyang-2, HY-2), it is urgent to explore the potential application of the HY-2B in Arctic sea ice thickness retrievals. In this study, we first derive the Arctic radar freeboard and sea ice thickness during two cycles (from October 2019 to April 2020 and from October 2020 to April 2021) using HY-2B radar altimeter and compare the results with the Alfred Wegener Institute (AWI) CS-2 products. We evaluate our HY-2B sea ice freeboard and thickness products using Operation IceBridge (OIB) airborne data and ICESat-2 products. Finally, we estimate the uncertainties in the HY-2B sea ice freeboard and sea ice thickness. The radar freeboard deviation between HY-2B and CS-2 is within 0.02 m, whereas the sea ice thickness deviation between HY-2B and CS-2 is within 0.2 m. The HY-2B radar freeboards are generally thicker than AWI CS-2, except in spring (March and April). In spring, more of the lowest 15 points within 25 km segment are likely to originate from floes, while more points may originate from leads in early winter. We also find that the deviations of radar freeboard and sea ice thickness between HY-2B and CS-2 over MYI are larger than over FYI. The correlation between HY-2B sea ice freeboard retrievals and OIB values is 0.77, with a a root mean square error (RMSE) is 0.13 m and a mean absolute error (MAE) is 0.12 m. The correlation between HY-2B sea ice thickness retrievals and OIB values is 0.65, with a RMSE is 1.86 m and a MAE is 1.72 m. The HY-2B sea ice freeboard uncertainty values range from 0.021 m to 0.027 m, while the uncertainties in the HY-2B sea ice thickness range from 0.44 m to 0.67 m.

删除[董昭顷]: of great significance

删除[董昭顷]: values

## 1 Introduction

25 Arctic sea ice is an important factor of the global climate system and plays an important role in maintaining its energy balance. By reflecting most of the solar shortwave radiation, sea ice reduces the absorption of solar shortwave radiation by seawater and blocks outward longwave radiation from leaving the ocean, thus regulating the overall radiation budget of the Earth. Sea ice also regulates the exchanges of heat, momentum and water vapour between the polar atmosphere and oceans (Thomas et al., 2010; Xu et al., 2017). Due to the special air-ice-sea feedback mechanism, the Arctic has exhibited warming temperatures at more than twice the global average increasing rate. This phenomenon is known as the "Arctic amplification" (Serreze et al., 2009). Studies have shown that global warming has led to decreases in the extent and thickness of Arctic sea

删除[董昭顷]: , D. N

删除[董昭顷]: effect

ice and that the ice age of multiyear ice has gradually decreased (Comiso et al., 2008; Lindell et al., 2016; Kwok, 2018; IPCC, 2019; Meier et al., 2022). Models predict that the Arctic will be ice-free in summer by the middle of the 21st century (Notz et al., 2020). The predicted decrease in Arctic sea ice will also change the living environment of Arctic mammals, and these changes will not be conducive to the survival or development of Arctic mammals, such as polar bears and walrus (IPCC, 2019). Due to the rapid retreat of sea ice, trans-Arctic shipping routes have become increasingly navigable (Stephenson et al., 2015; Cao et al., 2022). At the same time, the reduction in Arctic sea ice has improved the convenience of exploiting natural resources in the Arctic, and these activities will have an important impact on the economy of the Arctic and on regions beyond the Arctic.

Sea ice thickness, as the third dimension of sea ice, can be combined with sea ice extent to calculate sea ice volume to better understand changes in sea ice. However, sea ice thickness is also a difficult parameter to measure. The recent development of satellite altimeters has made it possible to obtain sea ice thickness over continuous and large ranges. To date, the available international altimeter satellites that obtain polar sea ice thickness observations include the European Remote Sensing Satellite 1 (ERS)-1, ERS-2, Envisat, Ice, Cloud and land Elevation Satellite (ICESat), CryoSat-2 (CS-2), Saral, Sentinel-3A, Sentinel-3B and ICESat-2 (IS-2). Laxon et al. (2003) derived Arctic sea ice thickness for the first time with the ERS-1/2 altimeter and verified their findings with submarine sonar data, thus confirming the feasibility of using satellite altimeters to retrieve sea ice thickness. Kwok et al. (2004) derived the Arctic sea ice thickness for the first time in 2004 using the Geoscience Laser Altimeter System (GLAS) on the ICESat satellite, further demonstrating the advantage of altimeter data in estimating Arctic sea ice thickness. Giles et al. (2008) estimated the Arctic sea ice thickness using the Envisat altimeter and analysed its variation pattern in winter from 2002 to 2007; the authors found that the area where the sea ice thickness showed a decreasing and thinning trend was mainly in the Beaufort Sea. Tilling et al. (2016) released near-real-time CS-2 sea ice thickness products with time periods of 2, 14 and 28 days. Also based on CS-2 data, Ricker et al. (2014) set threshold ranges for the pulse peak (PP), stack standard deviation (SSD) and stack kurtosis (K) terms to separate the lead, sea ice and open water, compared and analysed the effects of different retracking thresholds on the sea ice thickness, and estimated the uncertainties of the sea ice freeboard and sea ice thickness. Shen et al. (2020) used Sentinel-3A to retrieve Arctic sea ice freeboard and analysed the difference and consistency between Sentinel-3A and CS-2. The results showed that the Sentinel-3A sea ice freeboard was generally lower than that retrieved by CS-2. The differences between Sentinel-3A and CS-2 are mostly a result of the processing chain of Sentinel-3 not having included zero-padding or Hamming-weighting. The study of Lawrence et al. (2019) in which these corrections were applied showed greater consistency. Petty et al. (2020) generated monthly IS-2 sea ice thickness products and compared them with various monthly sea ice thickness estimates obtained from the European Space Agency (ESA)'s CS-2 satellite mission, with IS-2 showing consistently lower thicknesses. With the continuous progress of Arctic sea ice remote sensing technologies, a wide variety of sea ice thickness products have become available to the scientific community (Sallila et al., 2019). CS-2 radar altimeters, ICESat and IS-2 laser altimeters cover almost the entire Arctic Ocean due to their large orbital inclinations and are thus the main data sources for estimating sea ice thicknesses. However, few reports have explored the retrieval of sea ice thickness by Chinese altimeters among recent

删除[董昭顷]: As sea ice melts, large amounts of fresh water will be injected into the deep convection area of the North Atlantic Ocean, reducing the strength of the Atlantic meridional overturning circulation (AMOC) and thus transporting heat northwards towards the Arctic; in turn, this will lead to persistent anomalies in the sea ice extent (Liu et al., 2018; Halloran et al., 2020).

设置格式[董昭顷]: 非突出显示, 删除线

删除[LENOVO]: density

删除[董昭顷]: area

删除[董昭顷]: estimate

删除[董昭顷]: data

删除[董昭顷]: estimate

删除[董昭顷]: es

删除[董昭顷]: components

删除[董昭顷]: d

删除[董昭顷]: data based on Sentinel-3A records

删除[董昭顷]: s

删除[董昭顷]: the results

删除[董昭顷]: the corresponding

删除[董昭顷]: data

删除[董昭顷]: The results showed that the Sentinel-3A sea ice freeboard was generally lower than that indicated by CS-2.

删除[董昭顷]:

studies of polar sea ice thickness. [Jiang et al. \(2022\)](#) preliminarily estimated the Arctic radar freeboard from October 2020 to April 2021, compared them with radar freeboard products from the Alfred Wegener Institute (AWI). The overall difference between the HY-2B radar freeboard estimates and the AWI data is  $0.088 \pm 0.057$  m. The radar freeboards are generally higher for HY-2B than CS-2. With the continuous development of China's Marine Dynamic Environment Satellite (Haiyang-2B, HY-2B), the HY-2B satellite can be used to observe polar sea ice.

In this study, we use the HY-2B radar altimeter to retrieve Arctic radar freeboard and sea ice thickness and compare the results with the CS-2 products released by the AWI during the same period. Finally, we compare the results with Operation IceBridge (OIB) airborne data and IS-2 laser altimeter data. In Section 2, we introduce the data used in this study. In Section 3, we introduce the determination method of the sea surface height anomaly (SSHA) and the retrieval process of sea ice thickness in detail. In Section 4, we compare the Arctic HY-2B radar freeboard and sea ice thickness with AWI CS-2 products and IS-2 products. In Section 5, we discuss the influence of different SSHA determination schemes on the HY-2B radar freeboard and estimate the uncertainties in the HY-2B sea ice freeboard and sea ice thickness. Finally, in Section 6, we summarize the conclusions.

## 2 Study area and data

### 2.1 HY-2B radar altimeter

The HY-2B satellite was launched on October 25, 2018. It is China's second polar-orbiting marine dynamic environmental satellite and the second marine operational satellite in China's civil space infrastructure program. Its main mission is to monitor and survey the marine environment, obtain a variety of marine dynamic environmental parameters, including sea surface winds, wave heights, sea surface heights, sea surface temperatures and other elements, and take into account the observation of sea ice. The HY-2B satellite integrates both active and passive microwave remote sensors and carries loads such as a radar altimeter, microwave scatterometer, scanning microwave radiometer, correction radiometer, ship identification system and data collection system. [The HY-2B satellite adopts an orbit with a repeat cycle of 14 days in the early stage, and an orbit with a repeat cycle of 168 days in the late stage.](#) The HY-2B radar altimeter adopt the same reference ellipsoid of the TOPEX/Poseidon and the Jason-1/2/3. The HY-2B radar altimeter is a dual-band pulse-limited radar altimeter that comprised of the Ku band and C band to remove the impacts of ionospheric delays. Waveforms have been sampled to 128 range bins, each of which is 0.4864 m in range. Table 1 lists the main parameters of the HY-2B radar altimeter (Jiang et al., 2019; National Satellite Ocean Application Service, 2019).

The National Satellite Ocean Application Service (NSOAS) has released level-1, level-2 and fusion data products compiled through the pre-processing, data-retrieval and statistical averaging of the HY-2B altimeter level-0 data. The level-2 products are divided into Interim Geophysical Data Records (IGDR), Sensing Geophysical Data Records (SGDR) and Geophysical Data Records (GDR). [The SGDR products contain waveform data and have been re-tracked using the Brown model.](#) In addition, the HY-2B altimeter uses two different tracking modes: suboptimal maximum likelihood estimation (SMLE) and

设置格式[董昭顷]: 字体: (默认) Times New Roman, ...

删除[董昭顷]: as a supplementary means

删除[董昭顷]: Therefore, it is of great significance to ob ...

删除[董昭顷]: d

删除[董昭顷]: data

删除[董昭顷]: d

删除[董昭顷]: data

删除[董昭顷]: Alfred Wegener Institute (

删除[董昭顷]: )

删除[董昭顷]: d

删除[董昭顷]: data

删除[董昭顷]: data

删除[董昭顷]: data

删除[董昭顷]: results

删除[董昭顷]: radar

删除[董昭顷]: results

删除[董昭顷]: successfully

删除[董昭顷]: The HY-2B radar altimeter is a dual-band ...

删除[董昭顷]: The main parameters of the HY-2B radar ...

删除[董昭顷]: Because the SGDR product contains ...

offset center of gravity (OCOG). The two tacking modes can exchange according to the observation surfaces. The HY-2B Level-2 altimetry products (SGDR products) we used do not have OCOG data. Fig. 1 illustrates the spatial coverage of HY-2B SGDR data in April 2019.

删除[董昭顷]:

删除[董昭顷]: The spatial coverage of the HY-2B SGDR data in April 2020 is shown in Fig. 1.

## 2.2 CryoSat-2 radar altimeter

CS-2 was launched by the ESA in April 2010 with an orbital altitude of approximately 717 km, an orbital inclination of 92° and a repeat cycle period of 369 days. It has a 30-day sub-cycle and can realize monthly observations of the Arctic with a coverage of 88°N/S. CS-2 carries a Ku-band synthetic aperture interferometric radar altimeter (SIRAL) that can obtain the surface elevations of ground objects. Compared to conventional radar altimeters, CS-2 can achieve monthly observations of the Arctic with a coverage range of 88°N/S. This SIRAL uses delayed Doppler radar altimeter technology to reduce the satellite observation footprint to approximately 0.3 km along-track and 1.5 km across-track.

Currently, there are five main kinds of CS-2 sea ice thickness products: those from the ESA, the Centre for Polar Observation and Modeling (CPOM) (Laxon et al., 2003; Tilling et al., 2017), the AWI (Ricker et al., 2014; Hendricks et al., 2020), the National Snow and Ice Data Center (NSIDC) (Kurtz et al., 2014; Kurtz et al., 2017) and the ESA Climate Change Initiative (CCI) (Paul et al., 2018). These products are constructed using different retrack algorithms. Furthermore, the upcoming releases of CryoTEMPO are expected to be a favorable product to be used in the future by the science community.

删除[董昭顷]: four

删除[董昭顷]: and

删除[董昭顷]: sea ice freeboard retrieval

删除[董昭顷]: method

删除[董昭顷]: These products are constructed using different sea ice freeboard retrieval methods.

We mainly used the level-2 (L2) along-track data published by the ESA and the monthly average products published by the AWI.

删除[董昭顷]: I

删除[董昭顷]: sea ice thickness

## 2.3 ICESat-2 laser altimeter

The Advanced Terrain Laser Altimeter System (ATLAS) onboard IS-2 is a low-pulse energy laser (operating wavelength: 532 nm) that uses photon-counting technology to emit pulses at a repetition rate of 10 kHz (Degnan, 2002). The photon detector accurately calculates the round-trip time of these photons from the satellite to the ground and back to obtain distance measurements. We used the snow freeboard data of ATL20 products in the study (version 003 (Petty et al., 2021)); these products were provided by the National Aeronautics and Space Administration (NASA). The ATL20 snow freeboard was calculated by subtracting the local sea surface height (SSH) from the sea ice elevation. The average value of the specular reflected elevation of the inter-ice channel collected in the 10-km segment where the measurement point was located was used as the SSH estimation value (Kwok et al., 2021). The 10-km segments were selected to minimize the impact of the sea surface slope on the sea ice freeboard height estimations, as SSHs are generally constant within 10-km segments in polar regions north of 60°N. If SSH data were not available within a segment, the total freeboard estimate was not provided, thus assuring the reliability of the total freeboard estimates. Finally, the total freeboard height was gridded into a 25-km spatial grid, and the average value of the total freeboard height of all observation points in the grid was used as the total freeboard height of that grid. Assuming hydrostatic equilibrium, we used IS-2 snow freeboard products to calculate sea ice thicknesses with AWI snow depth products and compared with HY-2B and CS-2.

删除[董昭顷]: released

删除[董昭顷]:

删除[董昭顷]: Kacimi et al. (2022) used the IS-2 ATL10 snow freeboard product (version 004 (Kwok et al., 2021)), combined with the Arctic snow depths retrieved by obtaining the difference between IS-2 and CS-2 on the ice-snow reflection interface (Kwok et al., 2020), to retrieve Arctic monthly average sea ice thickness products. W

删除[董昭顷]: d

删除[董昭顷]: these

删除[董昭顷]: evaluate

删除[董昭顷]: sea ice thicknesses retrieved from

## 130 2.4 OIB airborne data

The airborne OIB experiment is an aerial remote sensing polar-region observation project started by NASA in 2009. Its initial purpose is to compensate for the data gaps that arise during the operation of ICESat and IS-2 satellites and to carry out large-scale sea ice detection experiments in the Arctic from March to May and in the Antarctic from October to November every year. Fig. 1 shows the flight path of the OIB in the Arctic in April 2019. In this study, we used IceBridge L4-level data (IDCSI4) to evaluate the sea ice freeboard and sea ice thickness retrieved by HY-2B and CS-2. In addition, we gridded the OIB data to a 25-km polar stereographic grid and set no fewer than 100 observation points inside each grid to optimally solve the limited representation problem of the OIB data.

删除[董 昭顷]: The flight path of the OIB in the Arctic in April 2019 is shown in Fig. 2.

删除[董 昭顷]: data

## 2.5 Auxiliary data

We used auxiliary data, including sea ice concentration (SIC), sea ice type, mean sea surface height (MSS), snow depth, and snow density in this study. The SIC (version OSI-401-b) and sea ice type (version OSI-403-b) data were released by the European Organization for Meteorological Satellites (EUMETSAT) Ocean and Sea Ice Satellite Application Facility (OSI-SAF). The MSS data were released by the Technical University of Denmark (DTU).

删除[董 昭顷]: In this study, we used auxiliary data, including data representing the sea ice concentration (SIC), sea ice type, mean sea surface (MSS) height, snow depth and snow density.

设置格式[董 昭顷]: 字体: 非加粗, 字体颜色: 红色, 非突出显示

删除[董 昭顷]: the Denmark Technical University

删除[LENOVO]: Tonboe

### 2.5.1 Sea ice concentration

Rasmus et al. (2016) used the brightness temperatures of the 19-V, 37-V and 37-H channels in the Special Sensor Microwave-Imager/Sounder (SSMIS) scanning radiometer to retrieve SICs with a hybrid algorithm constructed from the Bristol algorithm and bootstrap algorithm. To ensure optimum performances over both marginal and consolidated ice and to retain the virtues of each algorithm, the Bristol algorithm is given low weights at low concentrations, while the opposite is the case for high-ice-concentration regions (Rasmus et al., 2016). The SIC data are provided as a daily average grid product with the 10-km Lambert azimuthal grid. We used these SIC data to screen the altimeter data, and altimeter observations corresponding to areas with SICs greater than 70% were used in the sea ice freeboard calculations.

### 2.5.2 Sea ice type

We used sea ice type data to distinguish first-year ice (FYI) from multiyear ice (MYI). Signe et al. (2021) used the gradient ratio (GR) of 19/37 in Advanced Microwave Scanning Radiometer-2 (AMSR-2) microwave radiometer data and the scattering coefficient in the Advanced Scatterometer (ASCAT) microwave data to calculate the ice type probability. The sea ice type data are provided as a daily average grid product with a 10-km Lambert azimuthal grid.

删除[董 昭顷]:

删除[LENOVO]: ;

删除[董 昭顷]: remov

删除[LENOVO]: this model

删除[LENOVO]: can

### 2.5.3 MSS height

In this study, we employed the DTU18 MSS model to eliminate errors due to unresolved gravity features, intersatellite biases and remaining satellite orbit errors. After subtracting the MSS, we are able to precisely determine the instantaneous elevation



of lead (Skourup et al., 2017). The DTU18 MSS model is fused with the data of several satellite altimeters, such as TOPEX/Poseidon (T/P), Jason-1 (J1), Jason-2 (J2), ERS-1, ERS-2, ENVISAT, ICESat, Geosat, Geosat Follow-On (GFO) and CryoSat-2 (Andersen et al. 2018a; Andersen et al. 2018b).

#### 2.5.4 Snow depth

Hendricks et al. (2020) obtained a composite snow depth product (hereafter referred to as the AWI snow depth product) by fusing climatology snow depths from Warren et al. (1999, hereinafter W99), with the daily average AMSR-2 snow depths of the University of Bremen. To merge these two datasets, the authors created a monthly average AMSR-2 snow depth product to match the W99 climatology snow depths from October to April. They then low-pass filtered the monthly average AMSR-2 snow depths with a Gaussian filter with a size of 8 grid cells, removed negative snow depth values and limited the upper range to 60 cm. Finally, they created a regional weighting factor to ensure a smooth transition between the two types of data in the borderline area. Since the W99 climatology snow depths on FYI are higher, they had to be corrected by a coefficient of 0.5 (Kwok et al. 2015). However, the AMSR-2 snow depths on FYI did not need to be modified, so the authors introduced a total scaling factor to correct the contribution of W99 (Hendricks et al., 2020). The AWI snow depth products are provided as monthly averaged grid products using the Equal Area Scalable Earth Grid version 2 (EASE2) for the Northern Hemisphere with a spatial resolution of 25 km.

设置格式[董昭顷]: 字体: (默认) Times New Roman, 字体颜色: 红色, 非突出显示

删除[董昭顷]: W99 climatology snow depths

删除[董昭顷]: snow depth data are provided as a monthly averaged grid product in which the Equal Area Scalable Earth Grid version 2 (EASE2) is used for the Northern Hemisphere with a spatial resolution of 25 km.

删除[董昭顷]: Kwok et al. (2020) used the freeboard differences measured by IS-2 (by measuring the height between the local sea level and the air-snow interface) and CS-2 (by measuring the height between the local sea level and the snow-sea ice interface) to invert the snow depth data in the

#### 2.5.5 Snow density

To minimize differences in sea ice thicknesses at the beginning of the sea ice growing season, we used the evolving snow density values proposed by Mallett et al. (2020). These values are consistent with the snow densities used in the AWI CS-2 sea ice thickness product. The density equation of snow is shown in Equation (1).

$$\rho_s = 6.50t + 274.51 \quad (1)$$

where  $t$  represents the number of months since October.

设置格式[LENOVO]: 字体: (中文) 宋体, 非突出显示, 英语(美国), (中文) 中文(简体)

设置格式[LENOVO]: 字体: (中文) 宋体, 非突出显示, 英语(美国), (中文) 中文(简体)

删除[董昭顷]: The specific snow density values are shown in Table 2.

### 3 Method

In this section, we described the sea ice thickness retrieval method applied for the SGDR data of the HY-2B pulse-limited radar altimeter in detail and compared the parameters involved in the retrieval process with those in the CS-2 L2 along-track data released by the ESA.

设置格式[董昭顷]: 字体: (默认) Times New Roman, 非突出显示

设置格式[董昭顷]: 字体: (默认) Times New Roman, 字体颜色: 红色, 非突出显示

设置格式[董昭顷]: 左

#### 3.1 Retrieval process

The technical process of retrieving sea ice thickness based on HY-2B SGDR data is shown in Fig. 2. The specific retrieval process is as follows:

删除[董昭顷]: 1

删除[董昭顷]: 3

(1) ~~Nan values in the SGDR data and data south of 60°N were eliminated. Due to the influence of instrument noise, atmospheric factors and tidal factors during the propagation of pulse signals, it was necessary to consider the dry and wet tropospheric delay correction (National Centers for Environmental Prediction, NCEP), inverse barometric correction (NCEP), ionospheric correction (GIM), ocean tidal correction (Goddard Space Flight Center, GSFC, GOT4.10c), ocean load tidal correction (GSFC, GOT4.10c), earth tidal correction (Cartwright et al., 1973) and polar tidal correction (Wahr, 1985) when calculating the surface elevation (Zhang et al., 2022).~~

(2) ~~The SICs of data points in all HY-2B orbits were obtained using nearest interpolation. We used altimeter observations to calculate radar freeboard for areas with SIC greater than 70%. Sea ice was classified into FYI, MYI and ambiguous ice using sea ice type data, and ambiguous ice was not considered for the subsequent sea ice thickness retrievals.~~

(3) ~~The mean sea-surface (MSS) height product DTU18 (Andersen et al. 2018a; Andersen et al. 2018b) was subtracted from the geolocated surface elevations to remove the geoid fluctuations, that is, the derived relative elevations of ground objects  $h$  (Ollivier et al., 2012; Zhang et al., 2021). The residual error may be caused by the errors of orbit determination and different tracking algorithm. The residual of sea surface height was eliminated by subtracting the average value of every 25 km ( $h_{25km}$ ) along track (Kwok et al., 2007; Zhang et al., 2021), as shown in Eq. (2). In addition, the relative surface elevations,  $h_r$ , outside the range +1.0 m to -1.0 m are removed from processing, as shown in Fig. 3 (a) and (b). Eq. (2) can be expressed as follows:~~

$$h_r = h - h_{25km}, \quad (2)$$

where  $h_r$  is the relative surface elevation after eliminating residuals, unit: m,  $h$  is the relative elevation of ground objects, unit: m, and  $h_{25km}$  is the average value every 25 km, unit: m.

(4) ~~If more than or equal to 15 observation points were available per 25 km in the track data, the average of the 15 lowest values was taken as the SSHA. Otherwise, the SSHA was considered to be nan and nearest interpolation was performed along track. The SSHA was subtracted from the observed values  $h_r$  inside each 25-km segment to obtain radar freeboard height, as shown in Eq. (3) and Fig. 3 (b) and (c). Since the HY-2B SGDR product has been re-tracked for the Brown model (Zhang et al., 2022), we did not re-track it again in this study, Eq. (3) can be expressed as follows:~~

$$f_r = h_r - SSHA, \quad (3)$$

where  $f_r$  is the radar freeboard, unit: m,  $h_r$  is the relative surface elevation after eliminating the residual, unit: m, and  $SSHA$  is the sea surface height anomaly, unit: m.

(5) ~~Due to the attenuation of electromagnetic waves when they pass through snowpack, it is necessary to correct radar freeboard based on the AWI snow depth, as shown in Eq. (4) (Hendricks et al., 2020; Glissenaar et al., 2021). We assumed that the radar pulses penetrate through any snow cover on floes and scatter from the snow-ice interface, which has been shown in laboratory experiments where the snow cover on sea ice is cold and dry (Beaven et al., 1995; Tilling et al., 2017).~~

删除[董昭顷]: Invalid

删除[董昭顷]: National Satellite Ocean Application Serv ...

删除[LENOVO]: it was necessary to consider the dry and ...

删除[董昭顷]: the

删除[董昭顷]: interpolated

删除[董昭顷]: the SIC data

删除[LENOVO]: ;

删除[董昭顷]: sea ice

删除[LENOVO]: in this process, the altimeter observation ...

删除[董昭顷]: used

删除[董昭顷]:

删除[董昭顷]: The geoid fluctuations were eliminated by ...

删除[董昭顷]: In the case of orbit determination errors o ...

删除[LENOVO]: from the observation data every 25 km

删除[董昭顷]: the

删除[董昭顷]: 1

删除[LENOVO]: The relative surface elevation, <math> ...

删除[董昭顷]: 4

删除[董昭顷]: 1

删除[董昭顷]: 1

删除[董昭顷]: 9

删除[董昭顷]: 9

删除[董昭顷]: 0

删除[董昭顷]: All the observed values <math> ... inside e ...

删除[董昭顷]: the SSHA

删除[董昭顷]: the

删除[董昭顷]: 2

删除[董昭顷]: 4

Despite some evidence that the scattering horizon migrates as temperature rises (Willatt et al., 2010), Tilling et al. (2017) did not observe any bias in their thickness retrieval when compared to year-round ice draft data, and so they thought that the impact of this effect was not significant.

$$f = f_r + \left(\frac{c}{c_s} - 1\right) \cdot h_s, \quad (4)$$

where  $f$  is the sea ice freeboard, unit: m,  $f_r$  is the radar freeboard, unit: m, and  $h_s$  is the AWI snow depth, unit: m,  $c$  is the speed of light in vacuum,  $c_s$  is the speed of light through snow, parameterized by Eq. (5) (Ulaby et al., 1986).

$$c_s = c \cdot (1 + 5.1 \cdot 10^{-4} \rho_s)^{-1.5}, \quad (5)$$

where  $\rho_s$  is the snow density (Mallett et al., 2020).

(6) The sea ice freeboard data were converted to sea ice thickness data by assuming hydrostatic equilibrium, as shown in Eq. (6). To obtain monthly grid values, we averaged all thickness measurements within a 25 km radius of the centre of each grid cell, with all points receiving equal weighting:

$$T = \frac{\rho_w}{\rho_w - \rho_i} \cdot f + \frac{\rho_s}{\rho_w - \rho_i} \cdot h_s, \quad (6)$$

where  $T$  is the sea ice thickness, unit: m,  $\rho_w$  is the water density, and  $\rho_i$  is the sea ice density. We used a fixed FYI density estimate of  $916.7 \text{ kg m}^{-3}$  and an MYI density estimate of  $882 \text{ kg m}^{-3}$  (Alexandrov et al., 2010).

### 3.2 Comparison of along-track freeboard estimates

The orbit settings for HY-2B and CS-2 are different in that it is impossible to compare their radar freeboard estimates from the same position at the same time, so we compare the radar freeboard estimates of HY-2B and CS-2 on adjacent tracks within the Beaufort Sea, as shown in Fig. 4. Table 2 summarizes the mean and standard deviation values of the relative surface elevation, SSHA, and radar freeboard estimates based on HY-2B and CS-2. Fig. 4 (a) and (e) show the orbit positions of HY-2B and CS-2 obtained on April 4, 2020, and March 13, 2020, covering the Beaufort Sea and the northern Canadian Archipelago, respectively, to compare the relative surface elevation, SSHA, and radar freeboard estimates. In addition, both orbits cover the FYI (grey) and MYI (black) regions. Fig. 4 (b), (c), (f) and (g) show that the mean relative surface elevations of HY-2B and CS-2 in these two periods are  $0 \text{ m}/0 \text{ m}$  and  $0.081 \text{ m}/0.087 \text{ m}$ , respectively. We find that the relative surface elevations of HY-2B are slightly lower than that of CS-2, which may have been caused by the fact that not all points within the 25 km segment are leads. The mean SSHAs of HY-2B and CS-2 in the two periods are  $-0.21 \text{ m}/-0.11 \text{ m}$  and  $-0.051 \text{ m}/-0.069 \text{ m}$ , respectively. We find that the SSHAs estimated by HY-2B are lower than those estimated by CS-2, and the SSHA dispersions estimated by HY-2B are larger than that estimated by CS-2. These are may be caused by the error of orbit determination, different tracking algorithm and different derivation method of SSHA. Fig. 4 (d) and (h) show the radar freeboard estimates of HY-2B and CS-2 in the two periods, respectively. We find that the radar freeboard estimates of

删除[董昭顷]: we assumed that electromagnetic waves c

删除[董昭顷]: as shown in Eq. (3). Therefore, we used th

删除[董昭顷]:

删除[董昭顷]:

设置格式[董昭顷]: 段落间距段前: 0 磅, 段后: 0 磅

删除[董昭顷]:

删除[董昭顷]: 3

设置格式[董昭顷]: 字体: (默认) Times New Roman,

删除[董昭顷]: where <math>f</math> is the sea ice freeboard,

删除[董昭顷]: 4

设置格式[LENOVO]: 字体: (中文) 黑体, 字体颜色: 绿

设置格式[LENOVO]: 字体: (中文) 黑体, 字体颜色: 绿

设置格式[LENOVO]: 字体: (中文) 黑体, 字体颜色: 绿

删除[LENOVO]: We gridded the sea ice thickness to the

设置格式[LENOVO]: 字体: (中文) Times New Roma

删除[董昭顷]: 4

设置格式[董昭顷]: 字体: (默认) Times New Roman,

删除[董昭顷]: <math></math>

删除[董昭顷]: <math></math>

删除[董昭顷]: <math></math>

删除[董昭顷]: sea

删除[董昭顷]: 5

删除[董昭顷]: 3

删除[董昭顷]: 5

删除[董昭顷]: 5

删除[LENOVO]: ±

删除[LENOVO]: 0.31 m

删除[LENOVO]: ±0.25 m



HY-2B are larger than those of CS-2. The anomalous radar freeboards are directly related to the SSHAs and the relative surface elevation of the ice floes. In addition, the selected tracks from HY-2B and CS-2 are not totally overlapped, hence the freeboard differences are also induced from the location and time period differences between the two products.

删除[董昭顷]: There were some abnormally high values

删除[董昭顷]: In addition, because the tracks of HY-2B

删除[董昭顷]: data

删除[董昭顷]: verified the results using OIB airborne da

删除[董昭顷]: 6

删除[董昭顷]: were

删除[董昭顷]: red

删除[董昭顷]: red

删除[董昭顷]: were

删除[董昭顷]: April 2020

删除[董昭顷]: radar freeboard

删除[董昭顷]: radar freeboard

删除[董昭顷]: data

删除[董昭顷]: d

删除[董昭顷]: 2

删除[董昭顷]: 4

删除[董昭顷]: c

删除[董昭顷]: 1

删除[董昭顷]: 9

删除[董昭顷]: c

删除[董昭顷]: The HY-2B radar freeboards were genera

设置格式[LENOVO]: 字体: (中文) 黑体, 字体颜色:

删除[董昭顷]: The mean absolute error (MAE) between

设置格式[LENOVO]: 字体: (中文) 黑体, 字体颜色:

删除[LENOVO]: The smallest mean deviation was -2.4 e

设置格式[LENOVO]: 字体颜色: 红色, 非突出显示

设置格式[LENOVO]: 字体: (中文) 黑体, 字体颜色:

设置格式[LENOVO]: 字体颜色: 红色, 非突出显示

## 250 4 Results

In this section, we used the method proposed in Section 3 to retrieve the HY-2B radar freeboard and sea ice thickness during the two periods of interest (from October 2019 to April 2020 and from October 2020 to April 2021). We also compared the results with the CS-2 radar freeboard and sea ice thickness released by the AWI during the same periods and analysed the differences between the HY-2B and CS-2 products with regards to different sea ice types. Finally, we used airborne and satellite laser altimetry as a reference.

### 255 4.1 Comparison with AWI CS-2 radar freeboard data

Based on the HY-2B SGDR data, we analyse the HY-2B monthly average radar freeboard data collected from October 2019 to April 2020 while also comparing them with the AWI CS-2 radar freeboard recorded during the same period, as shown in Fig. 5. The spatial patterns of the HY-2B and CS-2 data are in broad agreement; that is, thicker radar freeboards occur north of the Canadian Archipelago, while thinner radar freeboards occur in other seas. Since the height of the lead is usually lower than the height of the adjacent floes, our method is reasonable to where there are more leads in the 25 km segment. Despite this good spatial consistency, the HY-2B radar freeboards are generally thicker than those of AWI CS-2, except in spring (March and April). In spring, more of the lowest 15 points within 25 km segment are likely to originate from floes while in early winter, more points may originate from leads. Therefore, the radar freeboards in spring are lower than those of CS-2. The mean deviations of radar freeboard between the HY-2B and the AWI CS-2 range from -0.035 m to 0.016 m from October 2019 to April 2020. The HY-2B radar freeboards are generally higher than those of AWI CS-2 in FYI region, and lower than those of AWI CS-2 in MYI region. More of the lowest 15 points within 25 km segment are likely to originate from floes in MYI region, more points may originate from leads in FYI region. Therefore, the radar freeboard in MYI region is lower than that of CS-2. The HY-2B's spatial coverage is limited to 81° N/S, while the CS-2's coverage is limited to 88° N/S, so monthly average radar freeboard derived from the HY-2B retrievals lacks observation data in the Arctic central region, and the HY-2B radar freeboard results are sparse in early winter (October 2019 to December 2019).

Table 3 shows the mean and modal radar freeboards of HY-2B and AWI CS-2 from October 2019 to April 2020 and from October 2020 to April 2021. For comparison, only the overlapping data points in the two satellite products are considered. The AWI CS-2 mean freeboards are larger than the CS-2 modal freeboards in all months (Schwegmann et al., 2016). The HY-2B mean freeboards are also thicker than the HY-2B modal freeboards in all months. However, despite the similarities between the two satellite products, there are also clear differences between them. The mean freeboard differences and modal freeboard differences in spring between HY-2B and CS-2 are both larger than in early winter. Table 3 also indicates that the

275

spring radar freeboard retrieved by our method is lower than that of CS-2. Moreover, the HY-2B radar freeboard has a smaller linear growth rate than the CS-2, which is also reflected in Fig. 7 (a).

To assess the deviations between the HY-2B and AWI CS-2 radar freeboards on various sea ice types, we list the differences in FYI, MYI and total sea ice between two satellite products in Table 4. The radar freeboard deviation between HY-2B and AWI CS-2 over MYI is larger than over FYI, with deviations of approximately 3 cm on FYI (positive) and 5 cm on MYI (negative). In addition, the mean deviations of radar freeboard between HY-2B and AWI CS-2 change from positive to negative over time. In March and April, the deviations between HY-2B and AWI CS-2 are negative on FYI, MYI and total sea ice, indicating that the HY-2B radar freeboards are smaller than those of AWI CS-2. In general, the HY-2B radar freeboards exhibit a mean absolute error (MAE) of approximately 0.02 m with respect to CS-2 (Table 4). We think that the MAEs may have been caused by the error of orbit determination, retracking algorithm and the accuracy of the extracted HY-2B SSHAs. It should be noted that the HY-2B SSHAs are slightly lower than those of the CS-2, the elevations of the floes are slightly higher than the CS-2, so the HY-2B radar freeboards are higher than those of the CS-2.

#### 4.2 Comparison of sea ice thickness with AWI CS-2 data

Fig. 6 shows the spatial comparison of Arctic sea ice thickness between the HY-2B and the AWI CS-2 from October 2019 to April 2020. The spatial patterns of the two sea ice thickness products exhibited broad agreement; thicker sea ice occur north of the Canadian Archipelago, while thinner sea ice occur in the Eurasian continental marginal sea and Baffin Bay. Both products show similar seasonal changes in which the Arctic sea ice thickness gradually thicken. Although the spatial distributions are consistent, the HY-2B sea ice thicknesses are thicker than that of the CS-2 except in spring (March and April). This is mainly due to the thicker HY-2B radar freeboards than those of the CS-2. The mean deviations of sea ice thickness between HY-2B and AWI CS-2 range from -0.259 m to 0.230 m from October 2019 to April 2020. Due to the lower radar freeboards in spring than those of CS-2, the sea ice thicknesses are also lower in spring than those of CS-2. The HY-2B sea ice thicknesses are generally higher than those of AWI CS-2 in FYI region, and lower than those of AWI CS-2 in MYI region. In all months, the MAEs of sea ice thickness between HY-2B and AWI CS-2 are within 0.9 m. The HY-2B sea ice thickness has a smaller linear growth rate than the CS-2, which is also reflected in Fig. 7 (b).

Table 5 lists monthly mean and modal sea ice thickness values derived from HY-2B and AWI CS-2 from October 2019 to April 2020 and from October 2020 to April 2021. For comparison, only the overlapping data points in the two satellite products are considered. The AWI CS-2 mean thicknesses are larger than modal thicknesses in all months. The HY-2B mean thicknesses are also thicker than modal thicknesses, except in December 2019 and November 2020. Due to the distribution of HY-2B sea ice thickness is close to Gaussian distribution, the modal maybe close to the mean, or even slightly greater than the mean. The HY-2B sea ice thicknesses are thicker than CS-2 in early winter, while CS-2 sea ice thicknesses are greater than HY-2B in spring. These results are related to the accuracy of the extracted HY-2B SSHAs. Except in February, March and April, the monthly mean HY-2B sea ice thicknesses are thicker than AWI CS-2. The HY-2B modal thicknesses are thinner than AWI CS-2, except in December 2019, November 2020 and December 2020.

删除[董 昭顷]: Fig. 7 shows the seasonal variation trends ...

删除[董 昭顷]: the

删除[董 昭顷]: monthly average radar freeboards

删除[董 昭顷]: 5

删除[董 昭顷]: deviation

删除[董 昭顷]: the

删除[董 昭顷]: radar freeboard

删除[董 昭顷]: the

删除[董 昭顷]: radar freeboard

删除[董 昭顷]: d

删除[董 昭顷]: with

删除[董 昭顷]: were

删除[董 昭顷]: were

删除[董 昭顷]: the

删除[董 昭顷]: radar freeboards

删除[董 昭顷]: ed

删除[董 昭顷]: deviation

删除[董 昭顷]: c

删除[董 昭顷]: the

删除[董 昭顷]: radar freeboards

删除[董 昭顷]: deviation

删除[董 昭顷]: Because the HY-2B SSHAs were lower th ...

删除[董 昭顷]: 8

删除[董 昭顷]: Arctic sea ice thickness

删除[董 昭顷]: sea ice thickness

删除[董 昭顷]: red

删除[董 昭顷]: red

删除[董 昭顷]: At the same time. b

To assess the deviations between the HY-2B and the AWI CS-2 sea ice thicknesses among various sea ice types, we list the deviations on FYI, MYI, and total sea ice, as listed in Table 6. On FYI, the HY-2B sea ice thicknesses are thicker than AWI CS-2, except in March and April. On MYI, the HY-2B sea ice thicknesses are thinner than AWI CS-2 in all months. In addition, the mean deviations of sea ice thickness between HY-2B and AWI CS-2 change from positive to negative over time. In general, the HY-2B sea ice thicknesses exhibit a MAE of approximately 0.2 m with respect to CS-2 (Table 6). The MAEs are directly affected by the accuracy of the retrieved radar freeboard values.

Fig. 7 shows the seasonal variation trends of HY-2B and AWI CS-2 radar freeboards and sea ice thicknesses during two sea ice growing cycles averaged over the overlapping regions. We calculate the average radar freeboard and sea ice thickness over the common area. The growth trend of the HY-2B radar freeboards is slower than those of the AWI CS-2. As shown in Fig. 7 (a), the HY-2B radar freeboards are higher than the AWI CS-2 in winter, while the opposite pattern is observed in spring. The seasonal trend of sea ice thickness is also similar to the radar freeboard. The growth rate of AWI CS-2 sea ice thickness is approximately twice that of HY-2B, as shown in Fig. 7 (b).

### 4.3 Comparison with OIB and IS-2 data

We use the HY-2B SGDR data collected in April 2019 to retrieve sea ice freeboard and sea ice thickness and compare the OIB airborne observation with HY-2B and AWI CS-2, as shown in Fig. 8. Because the HY-2B radar altimeter can cover only the 81°N/S region, only 13 grids could be evaluated when overlapped with the OIB airborne data collected in the same period. The correlation between HY-2B sea ice freeboard and OIB is 0.77, with a root mean square error (RMSE) is 0.13 m and a MAE is 0.12 m. The correlation between AWI CS-2 sea ice freeboard and OIB is 0.84, with a RMSE of 0.10 m and a MAE of 0.081 m. Based on hydrostatic equilibrium, we use the AWI snow depth data to convert sea ice freeboard into sea ice thickness, which is verified against OIB sea ice thickness, as shown in Fig. 8 (c) and (d). The correlation between HY-2B sea ice thickness and OIB is 0.65, with a RMSE of 1.86 m and a MAE of 1.72 m suggest that this underestimation could not only be attributed to HY-2B sea ice freeboard but maybe also to snow depth or other parameters. The correlation between AWI CS-2 sea ice thickness and OIB is 0.80, with a RMSE of 1.00 m and a MAE of 0.75 m. The majority of the spread in our HY-2B evaluation is caused by HY-2B underestimating sea ice thickness compared with OIB over thick ice.

IS-2 laser altimeters have a range that reaches the snow surface on sea ice and therefore are not impacted by the uncertain scattering horizons within snow layers (Magruder et al., 2020). The spatial resolution (approximately 11 m of the measurement footprint (Fons et al., 2021)) of these altimeters are much higher than those of CS-2 (approximately 0.3 km along-track and 1.5 km across-track) and HY-2B (approximately 1.9 km across-track), thus providing independent all-Arctic snow freeboard data that can be compared with the HY-2B and CS-2 retrievals. The IS-2 snow freeboard are subtracted from the AWI snow depths to obtain the IS-2 sea ice freeboard. To compare these values with IS-2 sea ice freeboard, we use AWI snow depth to perform a wave propagation speed correction for HY-2B and AWI CS-2 radar freeboard. Fig. 9 shows monthly comparisons of sea ice freeboard between HY-2B and IS-2 and between CS-2 and the IS-2 from October 2019 to April 2020 and from October 2020 to April 2021, respectively. The RMSEs obtained between HY-2B and IS-2 range from

删除[董昭顷]: Fig-9 shows the time series of the HY-2B

设置格式[董昭顷]: 非突出显示, 删除线

删除[董昭顷]: sea ice thickness

删除[董昭顷]: derived

删除[董昭顷]: 7

删除[董昭顷]: were

删除[董昭顷]: the

删除[董昭顷]: sea ice thicknesses

删除[董昭顷]: were

删除[董昭顷]: the

删除[董昭顷]: sea ice thicknesses

删除[董昭顷]: except

删除[董昭顷]: October 2020 and November 2020

删除[董昭顷]: In addition, the deviation between the HY

删除[董昭顷]: had

删除[董昭顷]: deviation

删除[董昭顷]: the

删除[董昭顷]: sea ice thickness

删除[董昭顷]: This

删除[董昭顷]: deviation

删除[董昭顷]: was

删除[董昭顷]: mainly

设置格式[董昭顷]: 字体颜色: 红色, 非突出显示, 非删除线

删除[董昭顷]: 9

设置格式[董昭顷]: 字体颜色: 红色, 非突出显示, 非删除线

删除[董昭顷]: time

设置格式[董昭顷]: 字体颜色: 红色, 非突出显示, 非删除线

删除[董昭顷]: series

0.13 m to 0.16 m, and the MAEs range from 0.09 m to 0.12 m. The RMSEs between CS-2 and IS-2 range from 0.09 m to 0.12 m, and the MAEs range from 0.07 m to 0.10 m. We observe HY-2B to generate some significantly thicker sea ice freeboard than IS-2. The abnormal values from HY-2B may be caused by the error of orbit determination, the tracking algorithm of the Brown model and the determination algorithm of SSHA. In addition, the differences of measurement mode and footprint size maybe result the discrepancies between HY-2B and IS-2.

Assuming hydrostatic equilibrium, HY-2B and CS-2 sea ice freeboards are converted to sea ice thicknesses using AWI snow depth, and the results are compared with IS-2 sea ice thicknesses. Fig. 10 shows comparisons of the HY-2B and CS-2 sea ice thicknesses with the IS-2 sea ice thicknesses from October 2019 to April 2020 and from October 2020 to April 2021, respectively. The RMSEs of sea ice thickness derived between HY-2B and IS-2 range from 1.21 m to 1.48 m, and the MAEs range from 0.79 m to 1.00 m. The RMSEs derived between CS-2 and IS-2 range from 0.77 m to 0.93 m, and the MAEs range from 0.56 m to 0.74 m. The RMSE and MAE of sea ice thickness are thus related not only to sea ice freeboard and snow depth but also to sea ice type and snow density (Ricker et al., 2014).

## 5 Discussion

In this section, we first compared the effects of the SSHAs extracted under different parameter schemes on the HY-2B radar freeboard retrievals. We then discussed the uncertainties of the HY-2B sea ice freeboard and sea ice thickness.

### 5.1 Influence of different SSHA determination schemes on the HY-2B radar freeboard

Ricker et al. (2014) believed that the random uncertainty of radar freeboard can be determined by the speckle noise and actual accuracy of SSHAs. Therefore, it is crucial to accurately extract SSHAs in the HY-2B radar freeboard retrievals in this work. We adopt 8 schemes to determine these SSHAs and applied them to retrieve HY-2B radar freeboard. The specific parameter schemes are listed in Table 7. Moreover, the HY-2B radar freeboard retrievals are compared to the AWI CS-2 radar freeboard collected during the same period. The mean deviation, MAE and SSHA values retrieved between the two satellites under different schemes from October 2019 to April 2020 and from October 2020 to April 2021 are listed in Table 8. As the table shows (Schemes 1-8), the mean deviation and MAE values first decrease and then increase with the gradual increase in SSHA, indicating that a larger SSHA does not necessitate a smaller mean deviation or MAE. The SSHA values of Scheme 8 are largest, both are greater than -0.1 m. The mean deviations of gridded radar freeboard between HY-2B and CS-2 are all less than 0, indicating that the HY-2B radar freeboard retrievals are generally lower than the AWI CS-2 radar freeboards. In addition, the MAE of Scheme 8 is larger than that obtained under Scheme 7. Finally, according to the mean deviation and MAE values, we use Scheme 7 to extract SSHAs to retrieve the HY-2B radar freeboards. It is worth noting that the HY-2B radar freeboard and sea ice thickness retrieved by Scheme 7 result in slower growth rates compared to CS-2. In spring, more of the lowest 15 points within 25 km segment are likely to originate from floes, while more points may originate from leads in early winter. As a result, the errors of the retrieved HY-2B radar freeboard and sea ice thickness are

设置格式[LENOVO]: 字体: (中文) 黑体, 字体颜色: 红色, 非突出显示, (中文) 中文(简体)

设置格式[LENOVO]: 字体: (中文) 黑体, 字体颜色: 红色, 非突出显示, (中文) 中文(简体)

删除[LENOVO]: was



375 smaller in winter than in spring. Therefore, the HY-2B sea ice freeboard and sea ice thickness values are lower than those of CS-2 in spring, especially in March and April, as shown in Tables 3 and 5.

## 5.2 Uncertainty of HY-2B sea ice freeboard and sea ice thickness data

380 The speckle noise caused by instrument system errors is found to be  $\sigma_{SGDR} = 0.02 \text{ m}$  (National Satellite Ocean Application Service, 2019), and the SSHA uncertainty is assumed to be determined by the standard deviation of SSHAs within a moving 25-km window. The gridded uncertainty of radar freeboard can be expressed as shown in Eq. (7):

$$\hat{\sigma}_{I3,rf} = \sqrt{\frac{\sigma_{SSA}^2 + \sigma_{SGDR}^2}{n}}, \quad (7)$$

where  $\sigma_{SGDR} = 0.02 \text{ m}$ ,  $\sigma_{SSA}$  is the mean of these SSHA standard deviations, weighted by the number of SSHAs within a 25-km moving window,  $\hat{\sigma}_{I3,rf}$  is the gridded uncertainty of radar freeboard and  $n$  is the number of SSHAs within a 25-km grid cell.

385 The sea ice freeboard is calculated after a wave propagation speed correction has been applied to the radar freeboard. The gridded uncertainty of sea ice freeboard can be expressed as shown in Eq. (8):

$$\sigma_{I3,f} = \sqrt{\left(\left(\frac{c}{c_s} - 1\right) \cdot \bar{\sigma}_{h_s}\right)^2 + (\hat{\sigma}_{I3,rf})^2} \quad (8)$$

where  $\sigma_{I3,f}$  is the gridded uncertainty of sea ice freeboard,  $\bar{\sigma}_{h_s}$  is the gridded uncertainty of snow depth.

390 Finally, we calculated the partial derivative of Eq. (7) to obtain the weights of the single-variable variances to obtain the contribution of each variable to the thickness uncertainty, as shown in Eq. (9)-(12).

$$\frac{\partial T}{\partial f_r} = \frac{\rho_w}{\rho_w - \rho_i}, \quad (9)$$

$$\frac{\partial T}{\partial \rho_i} = \frac{f \cdot \rho_w + h_s \cdot \rho_s}{(\rho_w - \rho_i)^2}, \quad (10)$$

$$\frac{\partial T}{\partial h_s} = \frac{\rho_s}{\rho_w - \rho_i}, \quad (11)$$

$$\frac{\partial T}{\partial \rho_s} = \frac{h_s}{\rho_w - \rho_i}, \quad (12)$$

$$\sigma_f = \sqrt{\sigma_{SGDR}^2 + \sigma_{SSA}^2 + (0.22 \times \sigma_{h_s})^2}$$

删除[董昭顷]: 5

删除[董昭顷]: is the standard deviation of observation points within a 25-km moving window

删除[董昭顷]: <math></math>

删除[董昭顷]: <math></math>

删除[董昭顷]: sea ice

删除[董昭顷]: , and <math></math> is the AWI snow depth uncertainty.

删除[董昭顷]: sea ice

删除[董昭顷]: <math></math>

删除[董昭顷]: <math></math>

删除[董昭顷]: sea ice

删除[董昭顷]: sea ice

设置格式[董昭顷]: 字体: (中文) 黑体, 非突出显示, (中文) 中文(简体)

删除[董昭顷]:

删除[董昭顷]: 6

删除[董昭顷]: 7

删除[董昭顷]: 8

删除[董昭顷]:

删除[董昭顷]: 9



395 The sea ice thickness uncertainty can be divided into random uncertainty and systematic uncertainty. The speckle noise and sea surface height interpolation uncertainty are both defined as random error contributions (Hendricks et al., 2020). Ricker et al. (2014) hypothesized that the uncertainties of the modified W99 snow depth and snow density resulting from interannual variabilities are systematic and cannot be regarded as random uncertainty. However, the AWI snow depth product is a composite snow depth product obtained by integrating the W99 climatology snow depths and the daily average AMSR-2  
 400 snow depths of Bremen University. Therefore, we assumed that the uncertainties in the AWI snow depth and snow density products are systematic uncertainty. In addition, the density of snow and sea ice are also treated as systematic errors. Due to the variability in seawater density, the contribution of its uncertainty is ignored (Kurtz et al., 2014; Ricker et al., 2014). We calculated the mixed uncertainty of the sea ice thickness via Gaussian error propagation, as shown in Eq. (13):

$$\sigma_{I3,T} = \sqrt{\left(\frac{\bar{\rho}_w}{\bar{\rho}_w - \bar{\rho}_i} \cdot \sigma_{I3,f}\right)^2 + \left(\frac{f \cdot \bar{\rho}_w + \bar{h}_s \cdot \bar{\rho}_s}{(\bar{\rho}_w - \bar{\rho}_i)^2} \cdot \bar{\sigma}_{\rho_i}\right)^2 + \left(\frac{\bar{\rho}_s}{\bar{\rho}_w - \bar{\rho}_i} \cdot \bar{\sigma}_{h_s}\right)^2 + \left(\frac{\bar{h}_s}{\bar{\rho}_w - \bar{\rho}_i} \cdot \bar{\sigma}_{\rho_s}\right)^2} \quad (13)$$

405 where  $\sigma_{I3,T}$  is the gridded uncertainty of sea ice thickness,  $\bar{\sigma}_{\rho_i}$  is the gridded uncertainty of sea ice density,  $\sigma_{\rho_{FYI}} = 35.7 \text{ kg/m}^3$ ,  $\sigma_{\rho_{MYI}} = 23 \text{ kg/m}^3$ , and  $\sigma_{\rho_s} = 50 \text{ kg/m}^3$  (Alexandrov et al., 2010).

Fig. 11 shows the comparison of HY-2B sea ice freeboard uncertainty and AWI CS-2 sea ice freeboard uncertainty from October 2019 to April 2020 and October 2020 to April 2021. The spatial distributions of HY-2B sea ice freeboard uncertainty are similar with CS-2. The HY-2B sea ice freeboard uncertainties over MYI are greater than over FYI, as the  
 410 FYI snow depth and uncertainty values have been halved. In Table 9, we summarize the averages of sea ice freeboard uncertainty derived from HY-2B and CS-2 over the common area. The HY-2B sea ice freeboard uncertainty values range from 0.021 m to 0.027 m, while the CS-2 sea ice freeboard uncertainty values range from 0.022 m to 0.028 m.

Fig. 12 shows the comparison of the HY-2B sea ice thickness uncertainty and AWI CS-2 sea ice thickness uncertainty from October 2019 to April 2020 and from October 2020 to April 2021. The spatial distributions of the HY-2B sea ice thickness  
 415 uncertainty are also similar with CS-2. The HY-2B sea ice thickness uncertainties over MYI are greater than over FYI. In addition, the total error on HY-2B and CS-2 sea ice thickness estimates increases as ice thickness increases over the growth season. Snow depth is a major contributor to this growth in sea ice thickness error, as snow accumulates and the associated standard deviation of depth anomaly increases (Tilling et al., 2019). Over FYI in October, the sea ice thickness uncertainty generated by SSHA is a dominant contributor to the error budget for HY-2B and CS-2. As the growth season progresses, its  
 420 influence decreases as more measurements become available, and snow depth uncertainties become more significant. Over MYI, snow depth is the dominant contributing factor to the ice thickness error throughout the growth season for both HY-2B and CS-2 (Tilling et al., 2019). Table 10 summarizes the HY-2B sea ice freeboard uncertainty and CS-2 sea ice freeboard uncertainty over the common area. The HY-2B sea ice thickness uncertainties range from 0.44 m to 0.67 m, while the CS-2 sea ice thickness uncertainties range from 0.42 m to 0.69 m.

## 425 6 Conclusion

In this study, we first used Chinese HY-2B radar altimeter to estimate Arctic sea ice freeboard and sea ice thickness with a new retrieval method and then compared the results to the AWI CS-2 products recorded during the same period. The accuracy of the findings was verified with independent data sources including NASA OIB airborne data and IS-2 laser altimeter data. Finally, the uncertainties in the HY-2B sea ice freeboard and sea ice thickness were estimated. The main  
430 conclusions are as follows:

(1) The spatial distributions of the HY-2B radar freeboard and AWI CS-2 radar freeboard have good consistency, but there are still some differences in the numerical values and temporal evolution. The HY-2B radar freeboards are generally thicker than those of AWI CS-2, except in spring (March and April). In spring, more of the lowest 15 points within 25 km segment are likely to originate from floes while in early winter, more points may originate from leads. Therefore, the radar freeboards  
435 in spring are lower than those of CS-2. The mean deviations of radar freeboard between the HY-2B and the AWI CS-2 range from -0.035 m to 0.016 m from October 2019 to April 2020. The HY-2B radar freeboards are generally higher than AWI CS-2 in FYI region, and lower than AWI CS-2 in MYI region. More of the lowest 15 points within 25 km segment are likely to originate from floes in MYI region, more points may originate from leads in FYI region. Therefore, the radar freeboard in MYI region is lower than that of CS-2. Overall, the HY-2B radar freeboard are highly dependent on season and ice type. The  
440 radar freeboard deviation between HY-2B and AWI CS-2 over MYI is larger than over FYI, with deviations of approximately 3 cm on FYI (positive) and 5 cm on MYI (negative). In addition, the growth trend of the HY-2B radar freeboard is slower than AWI CS-2.

Similarly, the spatial distributions of the HY-2B sea ice thickness and AWI CS-2 data exhibited good consistency, but we still identified some differences in their numerical and temporal evolution patterns. The mean deviations of sea ice thickness  
445 between HY-2B and AWI CS-2 range from -0.259 m to 0.230 m from October 2019 to April 2020. Due to the lower radar freeboards in spring than those of CS-2, the sea ice thicknesses are also lower in spring than those of CS-2. In FYI region, the HY-2B sea ice thicknesses are generally higher than those of AWI CS-2, and lower than those of AWI CS-2 in MYI region. The sea ice thickness deviation between HY-2B and AWI CS-2 over MYI is larger than over FYI, with deviations of approximately 0.3 m on FYI (positive) and 0.4 m on MYI (negative). The HY-2B sea ice thickness also has a smaller linear  
450 growth rate than CS-2.

(2) Comparisons with the OIB obtained in April 2019 showed that the correlation between HY-2B sea ice freeboard retrievals and OIB values is 0.77, with a RMSE is 0.13 m and a MAE is 0.12 m. The correlation between HY-2B sea ice thickness retrievals and OIB values is 0.65, with a RMSE is 1.86 m and a MAE is 1.72 m. The majority of the spread in our HY-2B evaluation is caused by HY-2B underestimating sea ice thickness compared with OIB over thick ice. Moreover, the  
455 RMSEs between our HY-2B radar freeboard estimates and IS-2 range from 0.13 m to 0.16 m, and the MAEs range from 0.09 m to 0.12 m. The RMSEs between our HY-2B sea ice thickness estimates and IS-2 range from 1.21 m to 1.48 m, and

the MAEs range from 0.79 m to 1.00 m. The abnormal values from HY-2B may be caused by the error of orbit determination, Brown tracking algorithm and the determination algorithm of SSHA.

(3) Based on the Gaussian error propagation theory, we estimate the uncertainties in the HY-2B sea ice freeboard and sea ice thickness. The HY-2B sea ice freeboard uncertainty values range from 0.021 m to 0.027 m, while the uncertainties in the HY-2B sea ice thickness range from 0.44 m to 0.67 m. The HY-2B sea ice freeboard uncertainties over MYI are greater than over FYI, as the FYI snow depth and uncertainty values have been halved. The total error on HY-2B sea ice thickness estimates increases as ice thickness increases over the growth season. Snow depth is a major contributor to this growth in sea ice thickness error, as snow accumulates and the associated standard deviation of depth anomaly increases.

In this study, we preliminarily tried to use HY-2B radar altimeter to retrieve reliable Arctic sea ice thicknesses. However, the shortcoming of this work is that we did not accurately distinguish between floes and lead. We did not re-track the SGDR products since they have been re-tracked using the Brown model. In the future, we will develop a higher-accuracy classification algorithm to classify floes and lead and use this improved algorithm to retrieve sea ice freeboard and sea ice thickness. We will use an implementation of the Threshold First Maximum Retracker Algorithm (TFMRA) to estimate the range to the main scattering horizon for each waveform. In addition, the HY-2B SGDR data used in this work retained only the measurements of the suboptimal maximum likelihood estimation (SMLE) retracking algorithm, which is applicable only to the ocean surface. Although the offset centre of gravity (OCOG) retracking algorithm is applicable to non-ocean surfaces, including land and sea ice, it is not saved in SGDR data and thus needs to be obtained from HY-2B L1b data. It is necessary to recalculate the satellite altitude using fine-orbit determination data and recalculate various geophysical correction terms, including the wet and dry troposphere correction, ionospheric correction, ocean tidal correction, polar tide correction and earth tide correction terms. We will reprocess the HY-2B L1b data in the future to obtain more reliable polar sea ice thickness products.

*Data availability.* The HY-2B SGDR data are available at <ftp://osdds-ftp.nsoas.org.cn/>, provided by the NSOAS (last access: 30 June 2022). The radar freeboard and sea ice thickness data corresponding to CryoSat-2 Level 2I are available at <ftp://science-pds.cryosat.esa.int/>, provided by the ESA (last access: 30 June 2022). The CryoSat-2 radar freeboard, sea ice thickness, and snow depth data are available at [ftp://ftp.awi.de/sea\\_ice/](ftp://ftp.awi.de/sea_ice/), provided by the AWI (Ricker et al., 2014; Hendricks et al., 2020) (last access: 30 June 2022). The ATL20 products (version 003) for the ICESat-2 laser altimeter are available at <https://nsidc.org/data/ATL20/versions/3>, provided by the NSIDC (Petty et al., 2021) (last access: 30 June 2022). The IceBridge L4-level data (IDCSI4) are available at <https://nsidc.org/data/NSIDC-0708/versions/1/>, provided by the NSIDC (Kurtz et al., 2013) (last access: 30 June 2022). The sea ice concentration and sea ice type data are available at <https://osf-saf.eumetsat.int>, provided by the OSI-SAF (Rasmus et al., 2016; Signe et al., 2021) (last access: 30 June 2022). The DTU18 MSS data are available at <ftp://ftp.space.dtu.dk/pub/>, provided by the DTU (Andersen et al. 2018a; Andersen et al. 2018b) (last access: 30 June 2022).

删除[董昭顷]: The sea ice thickness error was related not only to the sea ice freeboard and snow depth values but also to the sea ice type and snow density.

删除[董昭顷]: Tonboe

*Author contributions.* Data curation, Z.D. Y.J. and L.S.; writing, Z.D. and L.S.; methodology, Z.D. L.S. M.L. Y.J. T.Z. and S.W.; validation, Z.D. T.Z. and S.W.; funding acquisition, L.S. and M.L. All authors have read and agreed to the published version of the manuscript.

495 *Competing interests.* The authors declare that they have no conflicts of interest.

*Acknowledgements.* The research is funded by the National Key Research and Development Program of China (grant numbers 2021YFC2803300 and 2018YFC1407200) and the Impact and Response of Antarctic Seas to Climate Change (grant number IRASCC2020-2022-No. 01-01-03).

500

## References

Alexandrov, V., Sandven, S., Wahlin, J., Johannessen, O.M.: The relation between sea ice thickness and freeboard in the Arctic, *The Cryosphere* 4, 373–380, <https://doi.org/10.5194/tcd-4-641-2010>, 2010.

505 Andersen, O. B., Knudsen, P., and Stenseng, L.: A New DTU18 MSS Mean Sea Surface—Improvement from SAR Altimetry, 172. In *Proceedings of the 25 years of progress in radar altimetry symposium*, Ponta Delgada, São Miguel Island, Portugal, 24–29 September 2018. Editors J. Benveniste and F. Bonnefond (Azores Archipelago, Portugal), 172, 24–26, 2018.

Andersen, O. B., Rose, S. K., Knudsen, P., and Stenseng, L.: The DTU18 MSS Mean Sea Surface Improvement from SAR  
510 Altimetry. In *International Symposium of Gravity, Geoid and Height Systems (GGHS) 2*, The second joint meeting of the International Gravity Field Service and Commission 2 of the International Association of Geodesy, Copenhagen, Denmark, 17–21, 2018.

Beaven, S.G., Lockhart, G.L., Gogineni, S.P., Hossetnmostafa, A.R., Jezek, K., Gow, A.J., Perovich, D.K., Fung, A.K.,  
515 Tjuatja, S., 1995. Laboratory measurements of radar backscatter from bare and snow covered saline ice sheets. *Int. J. Remote Sens.* 16 (4), 851–876, <https://doi.org/10.1080/01431169508954448>, 1995.

Cao, Y., Liang, S., Sun, L., Liu, J., Cheng, X., Wang, D., Chen, Y., Yu, M., Feng, K.: Trans-Arctic shipping routes expanding faster than the model projections, *Global Environmental Change*, Volume 73, 2022, 102488, ISSN 0959-3780,  
520 <https://doi.org/10.1016/j.gloenvcha.2022.102488>, 2022.

Cartwright, D. E., Edden, Anne C.: Corrected Tables of Tidal Harmonics, *Geophysical Journal International*, Volume 33, Issue 3, Pages 253–264, <https://doi.org/10.1111/j.1365-246X.1973.tb03420.x>, 1973.

525 Comiso, Josefino C., Parkinson, Claire L., Gersten, Robert, Stock, Larry.: Accelerated decline in the Arctic sea ice cover. *Geophysical Research Letters*, 35(1), L01703–. <https://doi.org/10.1029/2007gl031972>, 2008.

Degnan, J. J.: Photon-counting multikilohertz microlaser altimeters for airborne and spaceborne topographic measurements, *J. Geodyn.*, vol. 34, nos. 3–4, pp. 503–549, Oct. 2002, [https://doi.org/10.1016/s0264-3707\(02\)00045-5](https://doi.org/10.1016/s0264-3707(02)00045-5), 2002.

530

Fons, S. W., Kurtz, N. T., Bagnardi, M., Petty, A. A., & Tilling, R. L.: Assessing CryoSat-2 Antarctic snow freeboard retrievals using data from ICESat-2. *Earth and Space Science*, 8, e2021EA001728. <https://doi.org/10.1029/2021EA001728>, 2021.

535 Giles, K. A., Laxon, S. W., & Ridout, A. L.: Circumpolar thinning of Arctic sea ice following the 2007 record ice extent minimum. *Geophysical Research Letters*, 35(22). <https://doi.org/10.1029/2008gl035710>, 2008.

Glissenaar, I. A., Landy, J. C., Petty, A. A., Kurtz, N. T., and Stroeve, J. C.: Impacts of snow data and processing methods on the interpretation of long-term changes in Baffin Bay early spring sea ice thickness, *The Cryosphere*, 15, 4909–4927,

540 <https://doi.org/10.5194/tc-15-4909-2021>, 2021.

Hendricks, S., Ricker, R.: Product User Guide & Algorithm Specification—AWI CryoSat-2 Sea Ice Thickness (version 2.3). Available online: <https://www.researchgate.net/publication/346677382>, 2020.

545 IPCC.: Summary for Policymakers. In: IPCC Special Report on the Ocean and Cryosphere in a Changing Climate [H.-O. Pörtner, D.C. Roberts, V. Masson-Delmotte, P. Zhai, M. Tignor, E. Poloczanska, K. Mintenbeck, A. Alegría, M. Nicolai, A. Okem, J. Petzold, B. Rama, N.M. Weyer (eds.)]. In press, 2019.

Jiang, C., Lin, M., Wei, H.: A Study of the Technology Used to Distinguish Sea Ice and Seawater on the Haiyang-2A/B (HY-2A/B) Altimeter Data. *Remote Sensing*, 11(12), 1490. <https://doi.org/10.3390/rs11121490>, 2019.

550

Jiang, M., Xu, K., Zhong, W., Jia, Y.: Preliminary HY-2B Radar Freeboard Retrieval over Arctic Sea Ice. IGARSS 2022 - 2022 IEEE International Geoscience and Remote Sensing Symposium. <https://doi.org/10.1109/IGARSS46834.2022.9883529>, 2022.

555



Kurtz, N.T., Farrell, S.L., Studinger, M., Galin, N., Harbeck, J.P., Lindsay, R., Onana, V.D., Panzer, B., Sonntag, J.G.: Sea ice thickness, freeboard, and snow depth products from Operation IceBridge airborne data. *Cryosphere* 2013, 7, 1035–1056. <https://doi.org/10.5194/tc-7-1035-2013>, 2013.

560 Kurtz, N. T., Galin, N., Studinger, M.: An improved CryoSat-2 sea ice freeboard retrieval algorithm through the use of waveform fitting, *The Cryosphere*, 8, 1217–1237, <https://doi.org/10.5194/tc-8-1217-2014>, 2014.

Kurtz, N., Studinger, M. S., Harbeck, J., Onana, V., Farrell, S.: IceBridge Sea Ice Freeboard, Snow Depth, and Thickness in the Lincoln Sea, Northern Hemisphere, Tech. rep., Boulder, Colorado USA: NASA DAAC at the National Snow and Ice  
565 Data Center, 2012, updated 2014.

Kurtz, N. and Harbeck, J.: CryoSat-2 Level-4 Sea Ice Elevation, Freeboard, and Thickness, Version 1 [October–April, 2010–2018], NASA National Snow and Ice Data Center Distributed Active Archive Center, Boulder, Colorado USA, <https://doi.org/10.5067/96JO0KIFDAS8>, 2017.

570 Kwok, R.: ICESat observations of Arctic sea ice: A first look. *Geophysical Research Letters*, 31(16). <https://doi.org/10.1029/2004gl020309>, 2004.

Kwok, R., Cunningham, G. F., Zwally, H. J., Yi, D.: Ice, Cloud, and land Elevation Satellite (ICESat) over Arctic sea ice: Retrieval of freeboard. *Journal of Geophysical Research*, 112(C12), C12013–. <https://doi.org/10.1029/2006jc003978>, 2007.

575

Kwok, R., Cunningham, G. F.: Variability of Arctic sea ice thickness and volume from CryoSat-2. *Philosophical Transactions of the Royal Society A: Mathematical, Physical and Engineering Sciences*, 373(2045), 20140157–., <https://doi.org/10.1098/rsta.2014.0157>, 2015.

580 Kwok, R.: Arctic sea ice thickness, volume, and multiyear ice coverage: Losses and coupled variability (1958–2018). *Environmental Research Letters* 13(10):105005, <https://doi.org/10.1088/1748-9326/aae3ec>, 2018.

Kwok, R., Petty, A. A., Bagnardi, M., Kurtz, N. T., Cunningham, G. F., Ivanoff, A., and Kacimi, S.: Refining the sea surface identification approach for determining freeboards in the ICESat-2 sea ice products, *The Cryosphere*, 15, 821–833,  
585 <https://doi.org/10.5194/tc-15-821-2021>, 2021.

Lawrence, I. R., Armitage, T. W. K., Tsamados, M. C., Stroeve, J. C., Dinardo, S., Ridout, A. L., Muir, A., Tilling, R. L., Shepherd, A.: Extending the Arctic Sea Ice Freeboard and Sea Level Record with the Sentinel-3 Radar Altimeters. *Advances in Space Research*, <https://doi.org/10.1016/j.asr.2019.10.011>, 2019.

- 590 Laxon, S., Peacock, N., Smith, D.: High interannual variability of sea ice thickness in the Arctic region. *Nature*, 425(6961), 947–950. <https://doi.org/10.1038/nature02050>, 2003.
- Lindell, D. B. and Long, D. G.: Multiyear Arctic Sea Ice Classification Using OSCAT and QuikSCAT, *IEEE T. Geosci. Remote*, 54,167–175, <https://doi.org/10.1109/TGRS.2015.2452215>, 2016.
- 595 Magruder, L. A., Brunt, K. M., Alonzo, M.: Early ICESat-2 on-orbit geolocation validation using ground-based corner cube retro-reflectors. *Remote Sensing*, 12, 3653. <https://doi.org/10.3390/rs12213653>, 2020.
- Mallett, Robbie D. C., Lawrence, Isobel R., Stroeve, Julianne C., Landy, Jack C., Tsamados, Michel.: Brief communication: Conventional assumptions involving the speed of radar waves in snow introduce systematic underestimates to sea ice thickness and seasonal growth rate estimates. *The Cryosphere*, 14(1), 251–260. <https://doi.org/10.5194/tc-14-251-2020>, 2020.
- 600 Meier, W.N., J. Stroeve.: An updated assessment of the changing Arctic sea ice cover. *Oceanography*, <https://doi.org/10.5670/oceanog.2022.114>, 2022.
- 605 Notz, D., SIMIP Community.: Arctic sea ice in CMIP6. *Geophysical Research Letters* 47(10): e2019GL086749, <https://doi.org/10.1029/2019GL086749>, 2020.
- National Satellite Ocean Application Service (NSOAS):. Instructions for HY-2B Satellite Data. [https://osdds.nsoas.org.cn/HY2B\\_introduce](https://osdds.nsoas.org.cn/HY2B_introduce), 2019.
- 610 Ollivier, A., Faugere, Y., Picot, N., Ablain, M., Femenias, P., Benveniste, J. Envisat Ocean Altimeter Becoming Relevant for Mean Sea Level Trend Studies. *Marine Geodesy*, 35(sup1), 118–136. <https://doi.org/10.1080/01490419.2012.721632>, 2012.
- Paul, S., Hendricks, S., and Rinne, E.: Sea Ice Climate Change Initiative Phase 2, D2.1 Sea Ice Thickness Algorithm Theoretical Basis Document (ATBD), SICCI-P2-ATBD (SIT), v.1.0, 50 pp., available at: [https://admin.climate.esa.int/media/documents/Sea\\_Ice\\_Thickness\\_Algorithm\\_Theoretical\\_Basis\\_Document\\_1.0.pdf](https://admin.climate.esa.int/media/documents/Sea_Ice_Thickness_Algorithm_Theoretical_Basis_Document_1.0.pdf) (last access: September 2022), 2017.
- 615 Petty, A. A., Kurtz, N. T., Kwok, R., Markus, T., & Neumann, T. A.: Winter Arctic sea ice thickness from ICESat-2 freeboards. *Journal of Geophysical Research: Oceans*, 125, e2019JC015764. <https://doi.org/10.1029/2019JC015764>, 2020.
- 620

Petty, A. A., R. Kwok, M. Bagnardi, A. Ivanoff, N. Kurtz, J. Lee, J. Wimert, and D. Hancock.: ATLAS/ICESat-2 L3B Daily and Monthly Gridded Sea Ice Freeboard, Version 3. [Indicate subset used]. Boulder, Colorado USA. NASA National Snow and Ice Data Center Distributed Active Archive Center. <https://doi.org/10.5067/ATLAS/ATL20.003>, 2021.

625

Ricker, R., Hendricks, S., Helm, V., Skourup, H., Davidson, M.: Sensitivity of CryoSat-2 arctic sea-ice freeboard and thickness on radar-waveform interpretation. *Cryosphere* 2014, 8, 1607–1622. <https://doi.org/10.5194/tc-8-1607-2014>, 2014.

Rasmus, T., John, L.: The EUMETSAT OSI SAF Sea Ice Concentration Algorithm Theoretical Basis Document Product, OSI-401-b, Version 1.5. The Ocean and Sea Ice Satellite Application Facility, 2016.

630 Serreze, M. C., Barrett, A. P., Stroeve, J. C., Kindig, D. N., and Holland, M. M.: The emergence of surface-based Arctic amplification, *The Cryosphere*, 3, 11–19, <https://doi.org/10.5194/tc-3-11-2009>, 2009.

Stephenson, S.R., and L.C.Smith.: Influence of climate model variability on projected Arctic shipping futures, *Earth's Future*, 3331–343, <https://doi.org/10.1002/2015EF000317>, 2015.

635

Schwegmann, S., Rinne, E., Ricker, R., Hendricks, S., and Helm, V.: About the consistency between Envisat and CryoSat-2 radar freeboard retrieval over Antarctic sea ice, *The Cryosphere*, 10, 1415–1425, <https://doi.org/10.5194/tc-10-1415-2016>, 2016.

640

Skourup, H., Farrell, S. L., Hendricks, S., Ricker, R., Armitage, T. W. K., Ridout, A., Baker, S.: An assessment of state-of-the-art mean sea surface and geoid models of the Arctic Ocean: Implications for sea ice freeboard retrieval. *Journal of Geophysical Research: Oceans*, 122, 8593–8613. <https://doi.org/10.1002/2017JC013176>, 2017.

645 Sallila, H., Farrell, S. L., McCurry, J., and Rinne, E.: Assessment of contemporary satellite sea ice thickness products for Arctic sea ice, *The Cryosphere*, 13, 1187–1213, <https://doi.org/10.5194/tc-13-1187-2019>, 2019.

Shen, X., Ke, C., Xie, H., Li, M., Xia, W.: A comparison of Arctic sea ice freeboard products from Sentinel-3A and CryoSat-2 data. *International Journal of Remote Sensing*, 41(7), 2789–2806. <https://doi.org/10.1080/01431161.2019.1698078>, 2020.

650

Signe Aaboe, Emily Jane Down and Steinar Eastwood.: Algorithm Theoretical Basis Document for the Global sea-ice edge and type Product, GBL SIE OSI-402-d and GBL SIT OSI-403-d. The Ocean and Sea Ice Satellite Application Facility, 2021.

655 Thomas, D.N.; Dieckmann, G.S.: *Sea Ice*, 2nd ed.; Wiley-Blackwell: Oxford, UK, 2010.

Tilling, R. L., Ridout, A., and Shepherd, A.: Near-real-time Arctic sea ice thickness and volume from CryoSat-2, *The Cryosphere*, 10, 2003 – 2012, <https://doi.org/10.5194/tc-10-2003-2016>, 2016.

660 Tilling, R.L., Ridout, A., and Shepherd, A.: Estimating Arctic sea ice thickness and volume using CryoSat-2 radar altimeter data. *Adv. Space Res.*, <https://doi.org/10.1016/j.asr.2017.10.051>, 2017.

Tilling, R., Ridout, A., & Shepherd, A.: Assessing the impact of lead and floe sampling on Arctic sea ice thickness estimates from Envisat and CryoSat-2. *Journal of Geophysical Research: Oceans*, 124. <https://doi.org/10.1029/2019JC015232>, 2019.

665 Ulaby, F., Moore, R., and Fung, A.: *Microwave remote sensing: active and passive, Volume 3 – From Theory to Applications*, Artech House, Norwood, Massachusetts, USA, equation number: E.80, 1986.

Wahr, L.W.: Deformation of the earth induced by polar motion. *J. Geophys. Res.* 1985, 90, 9363–9368, <https://doi.org/10.1029/JB090iB11p09363>, 1985.

670

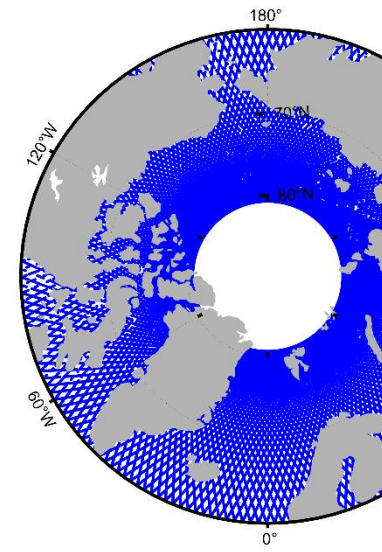
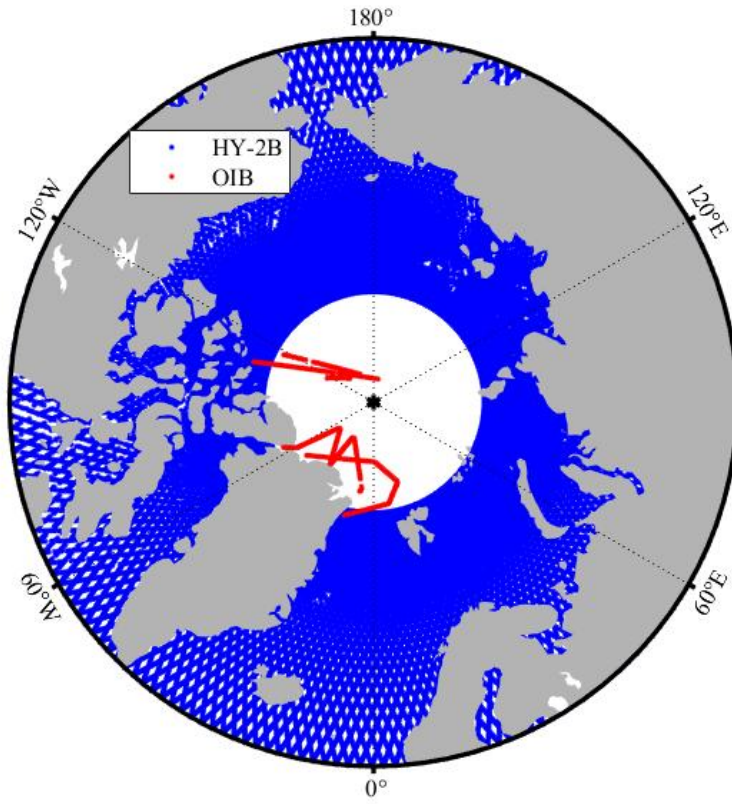
Warren, S.G., Rigor, I.G., Untersteiner, N., Radionov, V.F., Bryazgin, N.N., Aleksandrov, Y.I., Colony, R.: Snow Depth on Arctic Sea Ice. *J. Clim.* 1999, 12, 1814–1829. [https://doi.org/10.1175/1520-0442\(1999\)0122.0.co;2](https://doi.org/10.1175/1520-0442(1999)0122.0.co;2), 1999.

Willatt, R.C., Giles, K.A., Laxon, S.W., Stone-Drake, L., Worby, A.P.: Field investigations of Ku-band radar penetration  
675 into snow cover on Antarctic sea ice. *IEEE Trans. Geosci. Remote Sens.* 48 (1), 365–372, <https://doi.org/10.1109/TGRS.2009.2028237>, 2010.

Xu, S., Zhou, L., Liu, J., Lu, H., Wang, B.: Data Synergy between Altimetry and L-Band Passive Microwave Remote Sensing for the Retrieval of Sea Ice Parameters—A Theoretical Study of Methodology. *Remote Sensing*, 9(10), 1079.  
680 <https://doi.org/10.3390/rs9101079>, 2017.

Zhang, S.; Xuan, Y.; Li, J.; Geng, T.; Li, X.; Xiao, F.: Arctic Sea Ice Freeboard Retrieval from Envisat Altimetry Data. *Remote Sens.* 2021, 13, 1414. <https://doi.org/10.3390/rs13081414>, 2021.

685 Zhang, S.; Zhou, R.; Jia, Y.; Jin, T.; Kong, X.: Performance of HaiYang-2 Altimetric Data in Marine Gravity Research and a New Global Marine Gravity Model NSOAS22. *Remote Sens.* 2022, 14, 4322. <https://doi.org/10.3390/rs14174322>, 2022.

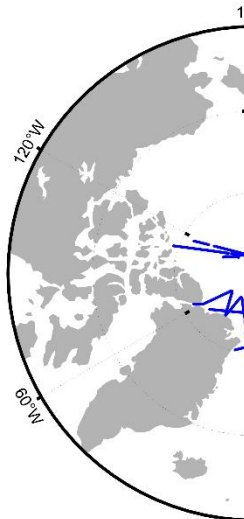


删除[董昭顷]:

删除[董昭顷]: :

删除[董昭顷]: An example of the accurate data

Figure 1. Ground tracks of HY-2B SGDR product (blue points) and Flight tracks of Operation IceBridge (OIB) airborne experiments (red points) across the Arctic in April 2019.



删除[董昭顷]:

删除[董昭顷]: Figure 2: Trajectory of the sea ice flight

690



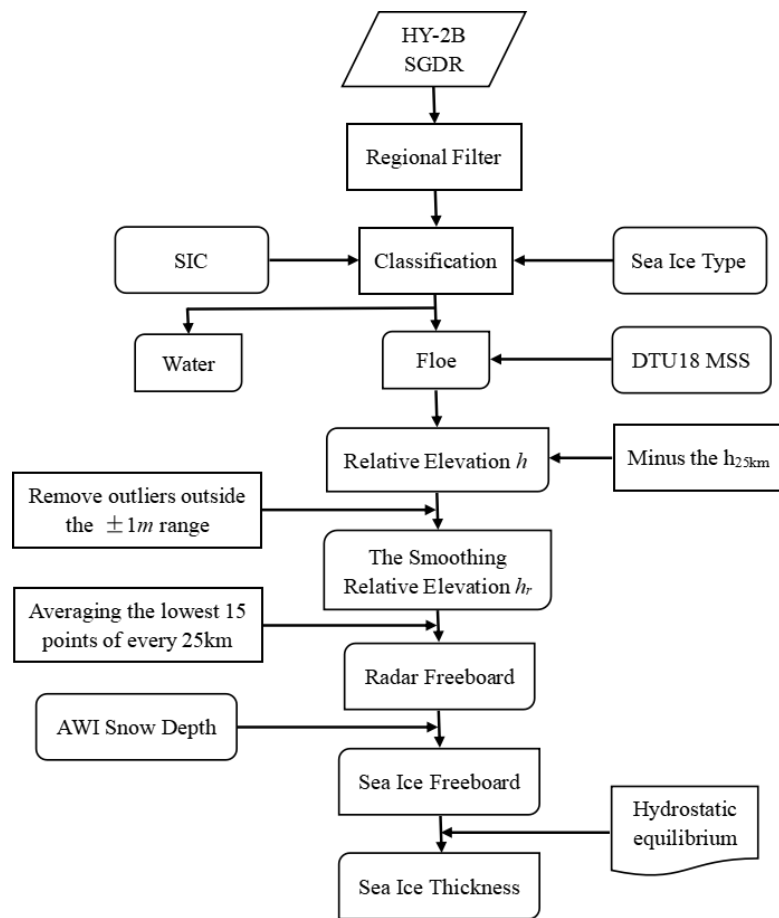
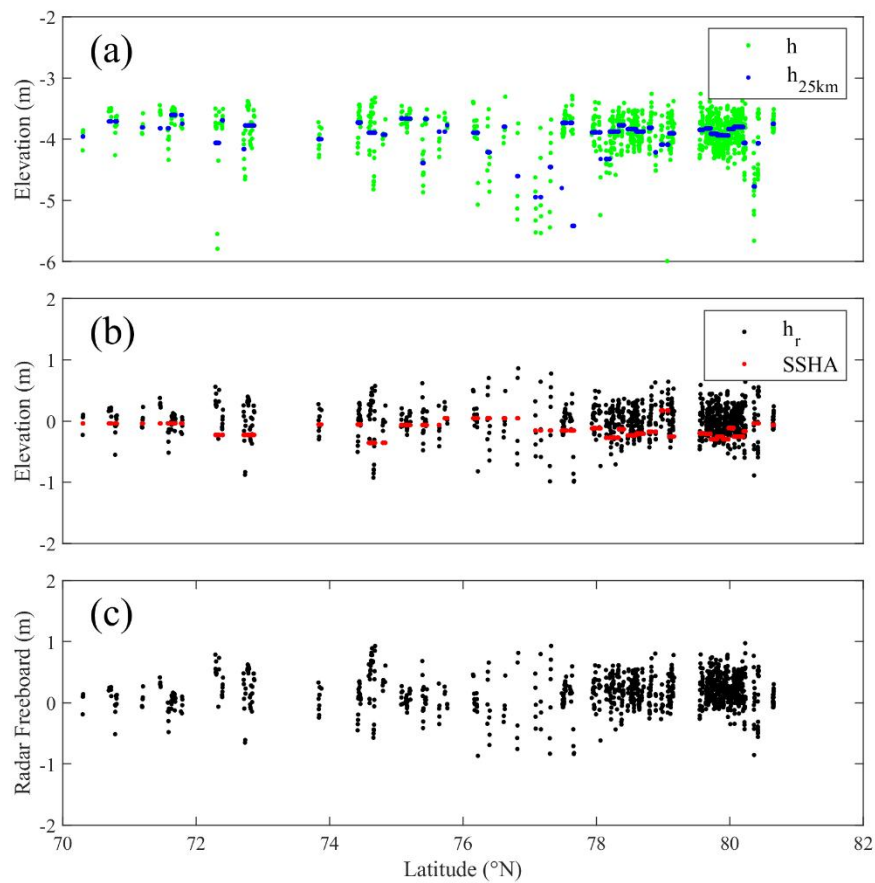
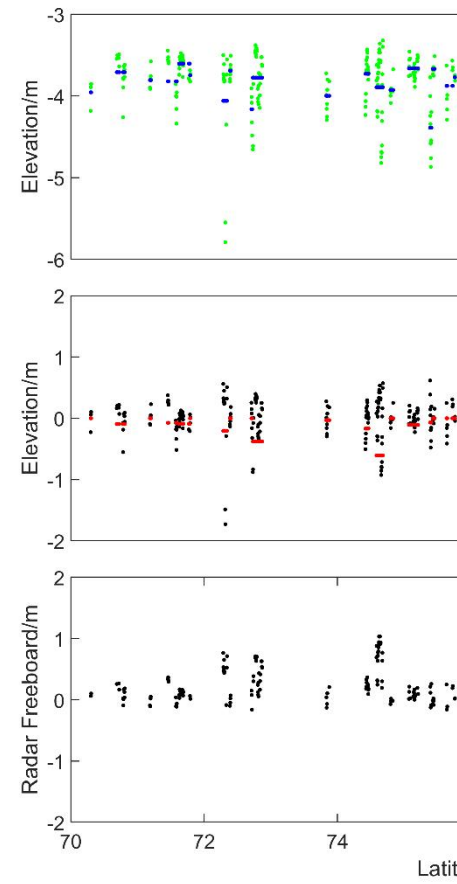


Figure 2. A flowchart of the sea ice thickness retrieval algorithm.

删除[董昭顷]: 3:

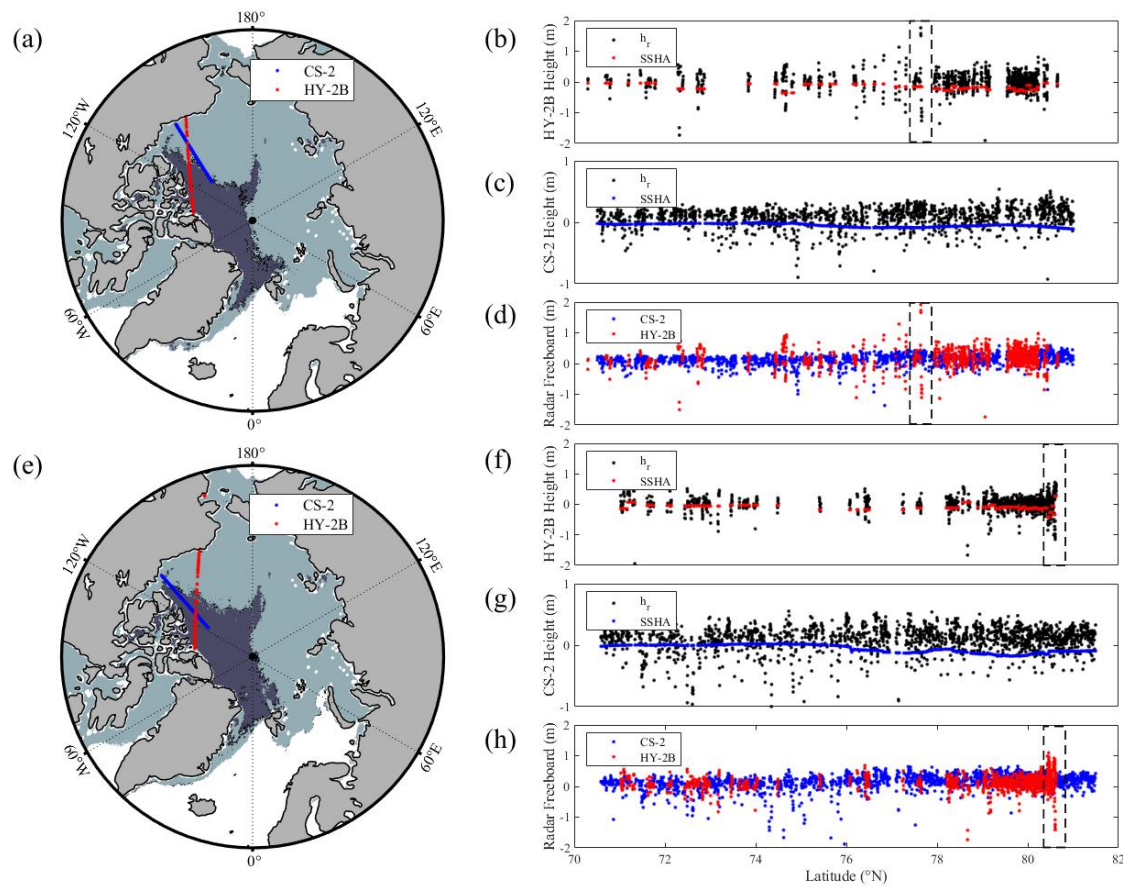


**Figure 3.** A sample of the HY-2B elevation profile obtained for of track number 14418 on April 4, 2020. The green points in panel (a) are the relative elevation ( $h$ ) values; the blue points in panel (a) are the  $h_{25km}$  values, defined as the 25-km running mean of  $h$ ; the black points in panel (b) are the modified relative elevation ( $h_r$ ) values; the red points in panel (b) are the sea surface height anomaly (SSHA) values; and the black points in panel (c) are the radar freeboard values.



删除[董 昭顷]:

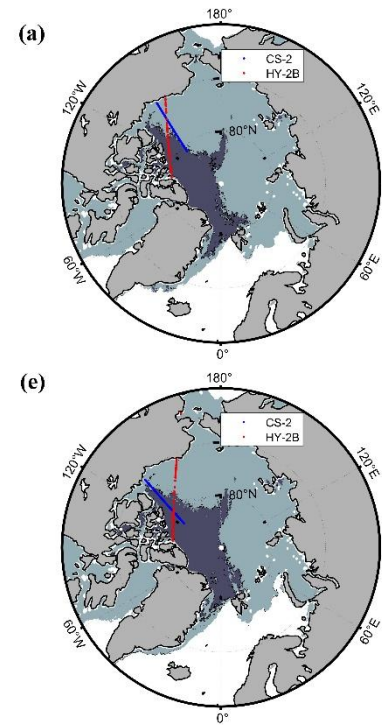
删除[董 昭顷]: 4:

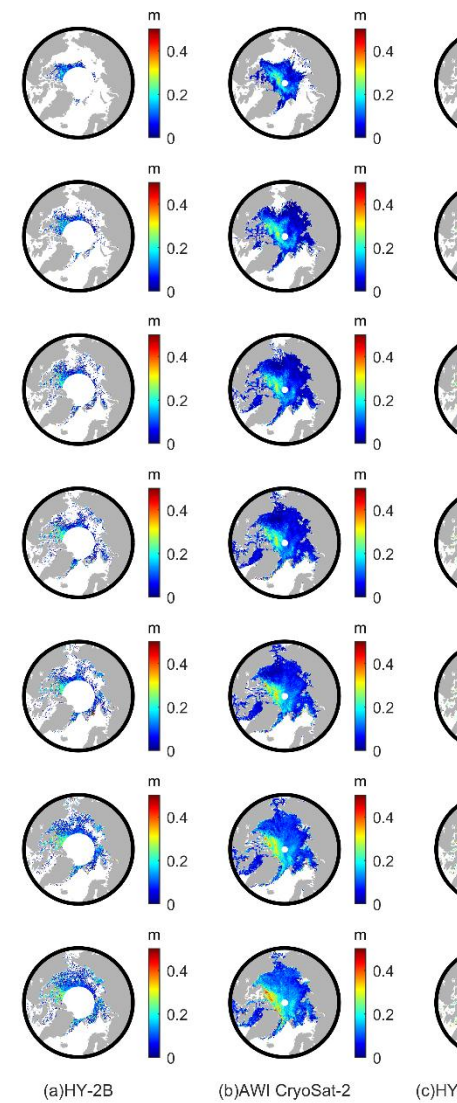
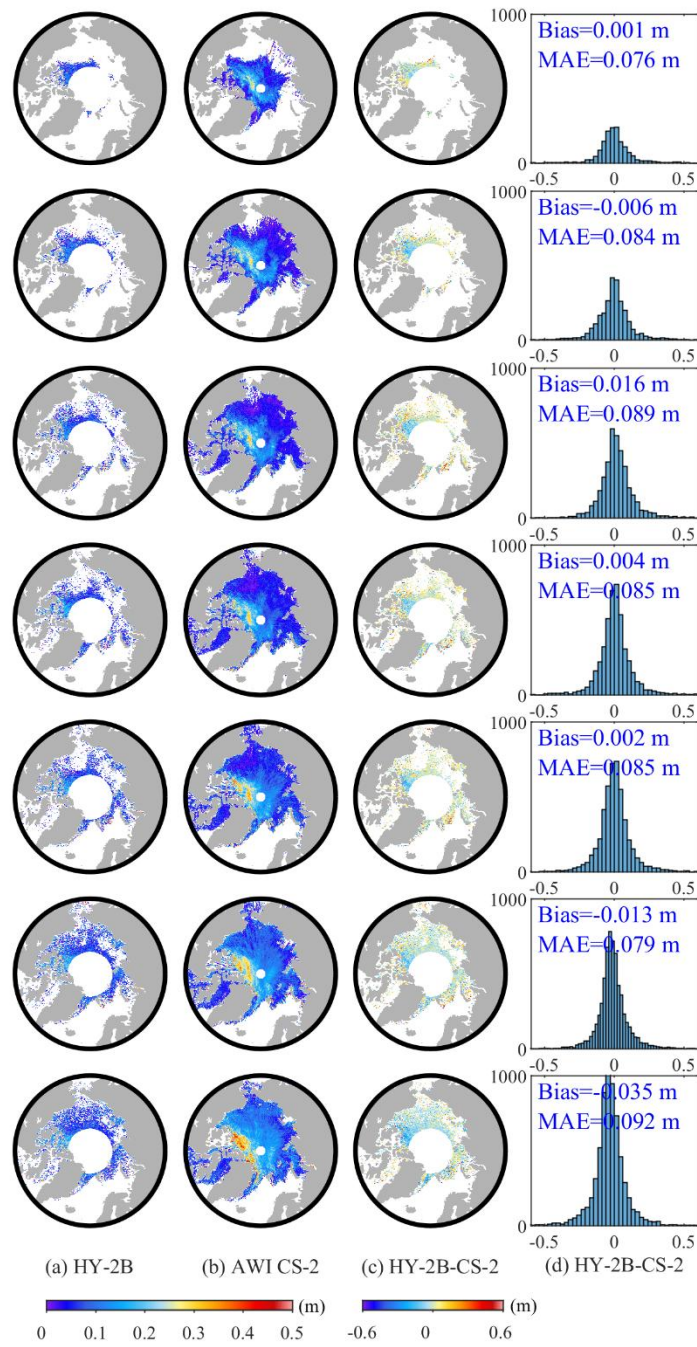


**Figure 4.** (a) (e) Cryosat-2 (blue) and HY-2B (red) tracks (acquired on April 4, 2020, and March 13, 2020, respectively) selected for comparison. FYI regions: light shading, MYI regions: dark grey shading. (b) (f) HY-2B relative surface elevations of floes (black dots) and SSHAs (red dots) corresponding to the tracks shown in panels (a) and (e), respectively. (c) (g) Cryosat-2 relative surface elevations of floes (black dots) and SSHAs (red dots) corresponding to the tracks shown in panels (a) and (e), respectively. (d) (h) Cryosat-2 (blue) and HY-2B (red) radar freeboard values corresponding to the tracks shown in panels (a) and (e), respectively.

删除[董昭顷]:

删除[董昭顷]: 5:

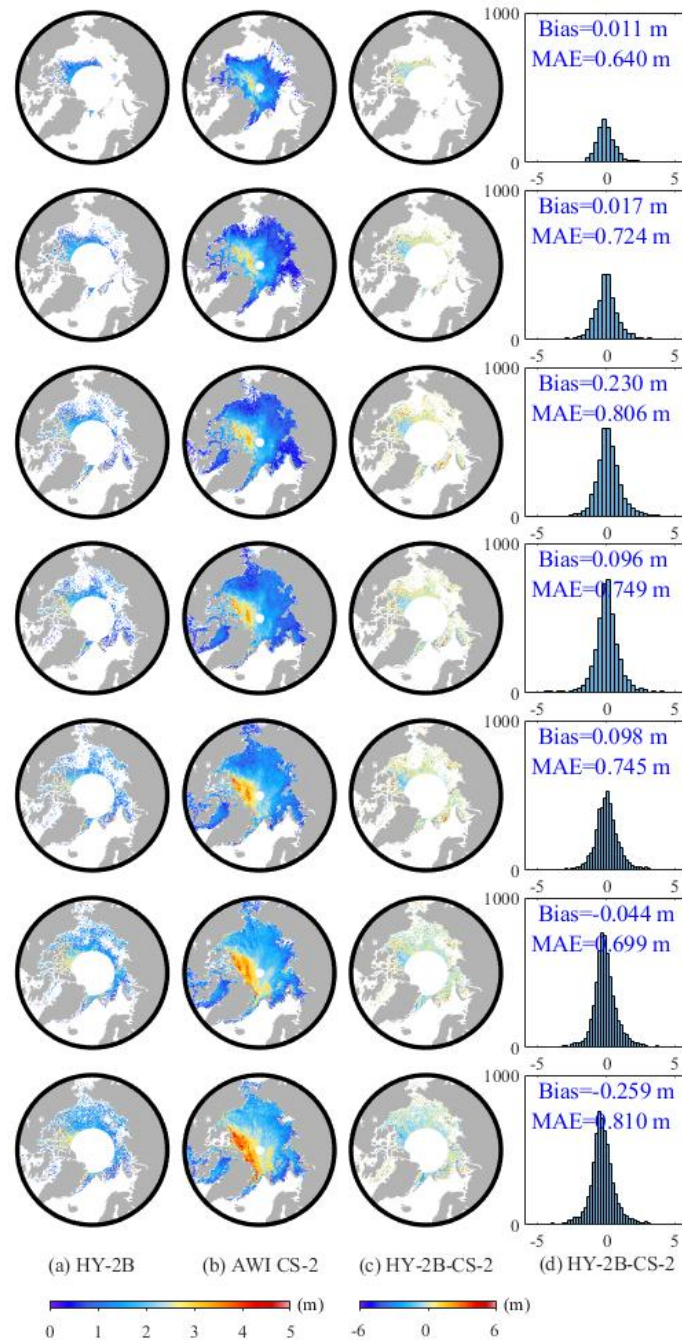




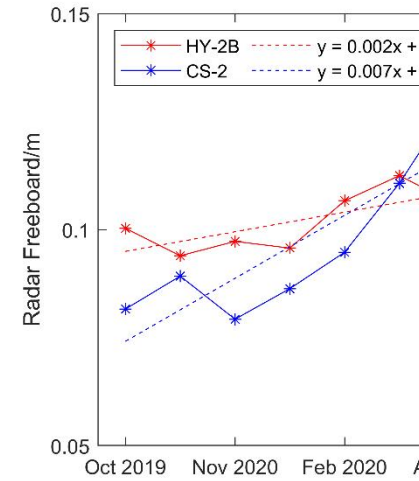
删除[董昭顷]:  
 删除[董昭顷]: 6  
 删除[董昭顷]: Cryosat  
 删除[董昭顷]: values  
 删除[董昭顷]: values  
 删除[董昭顷]: Cryosat  
 删除[董昭顷]: values  
 删除[董昭顷]: the  
 删除[董昭顷]: Cryosat  
 删除[董昭顷]: values

Figure 5. Comparisons and differences between HY-2B radar freeboard and AWI CS-2 radar freeboard, recorded from October 2019 to April 2020, (a) HY-2B radar freeboards, (b) CS-2 radar freeboards, (c) spatial differences between HY-2B and CS-2 radar freeboards, and (d) a histogram of differences between HY-2B and CS-2 radar freeboards.





**Figure 6.** Comparisons and differences between HY-2B sea ice thickness and AWI CS-2 sea ice thickness from October 2019 to April 2020, (a) HY-2B sea ice thicknesses, (b) CS-2 sea ice thicknesses, (c) spatial differences between HY-2B and CS-2 sea ice thicknesses, and (d) a histogram of the differences between HY-2B and CS-2 sea ice thicknesses.



删除[董昭顷]:

**Figure 7:** Seasonal variation trends of HY-2B and CryoSat-2 radar freeboard values from October 2019 to April 2020 and from October 2020 to April 2021.

删除[董昭顷]: 8:

删除[董昭顷]: Cryosat

删除[董昭顷]: values

删除[董昭顷]: Cryosat

删除[董昭顷]: Cryosat

删除[董昭顷]: Cryosat

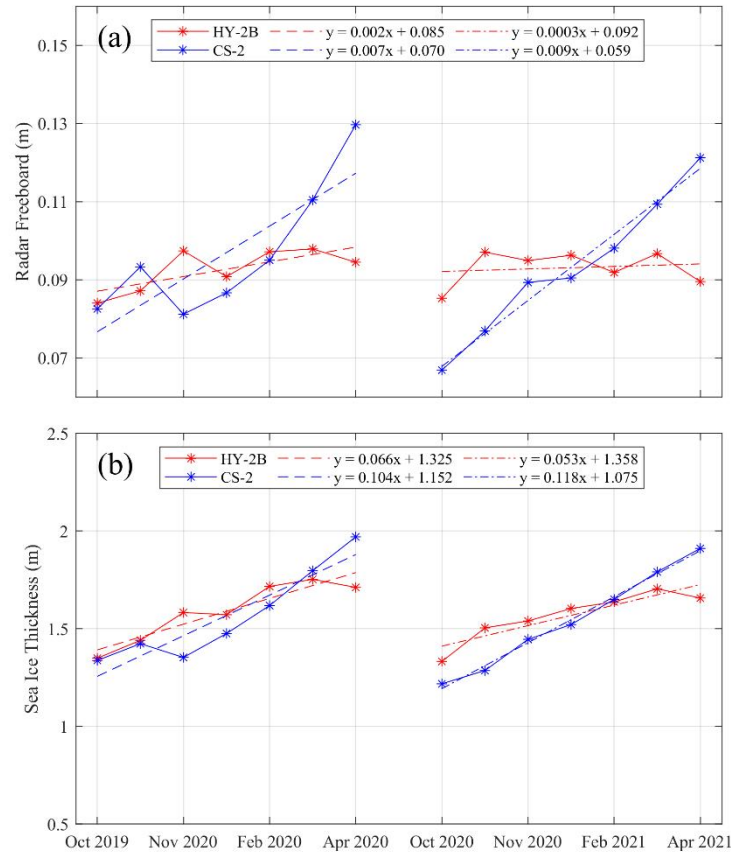
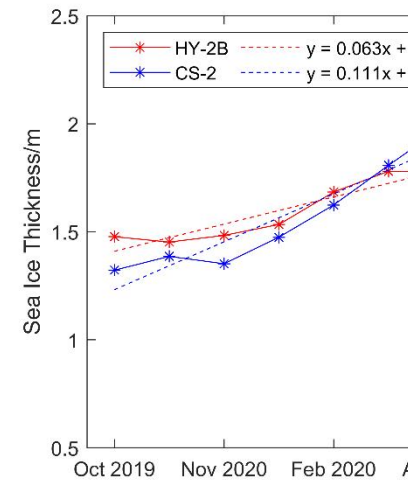


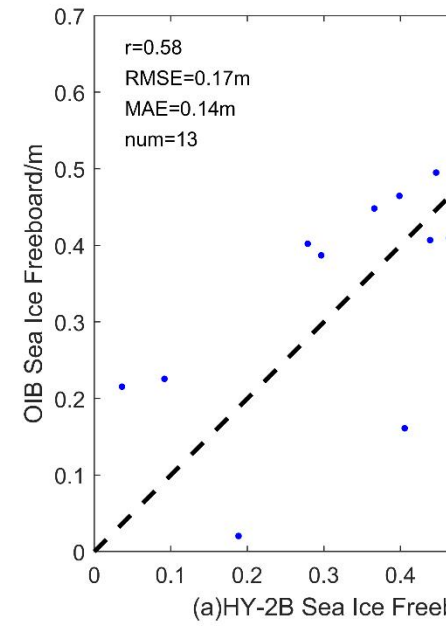
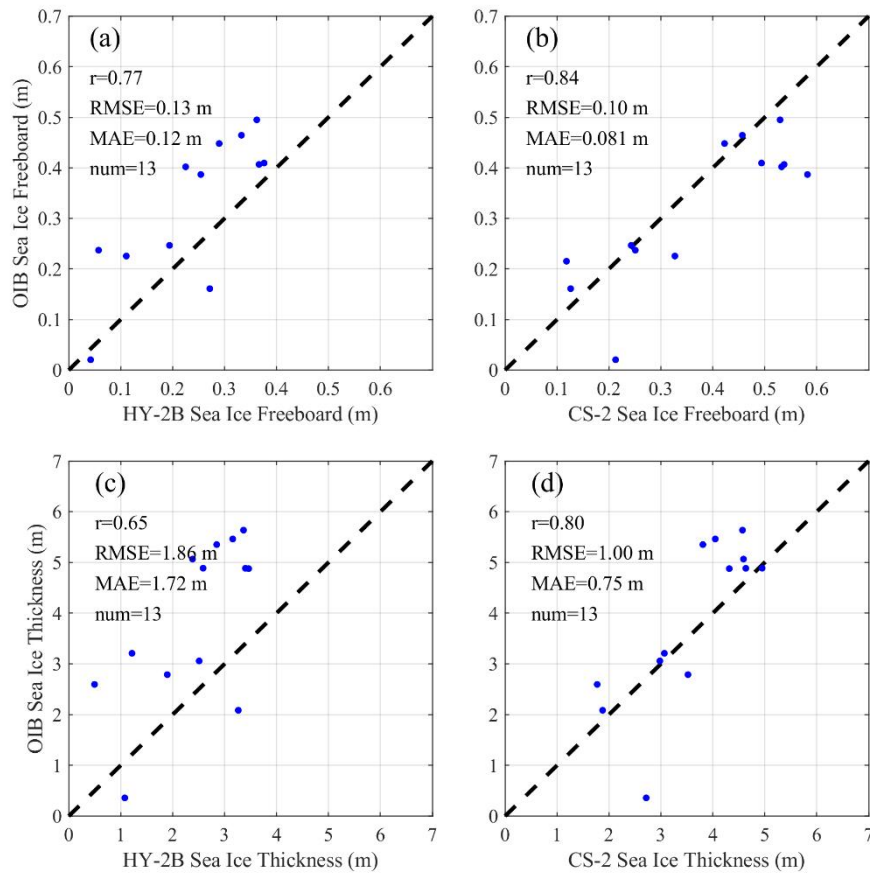
**Figure 7. Seasonal variation trends of HY-2B and CryoSat-2 radar freeboard and sea ice thickness from October 2019 to April 2020 and from October 2020 to April 2021. (a) radar freeboard, (b) sea ice thickness, HY-2B: red, CS-2: blue.**



删除[董昭顷]:

**Figure 9: Seasonal variation trends of HY-2B and CryoSat-2 sea ice thicknesses from October 2019 to April 2020 and from October 2020 to April 2021.**



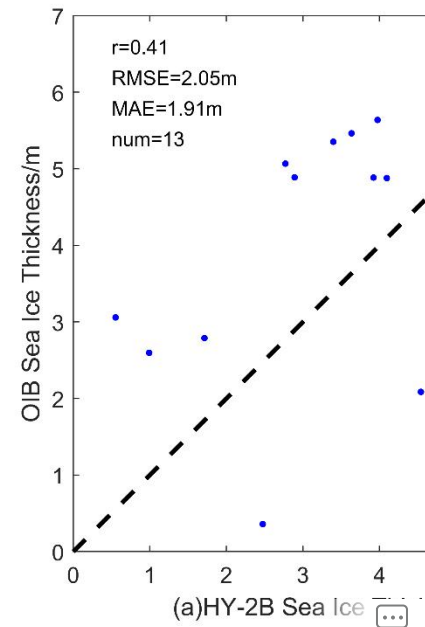


删除[董昭顷]:

删除[董昭顷]: 10:

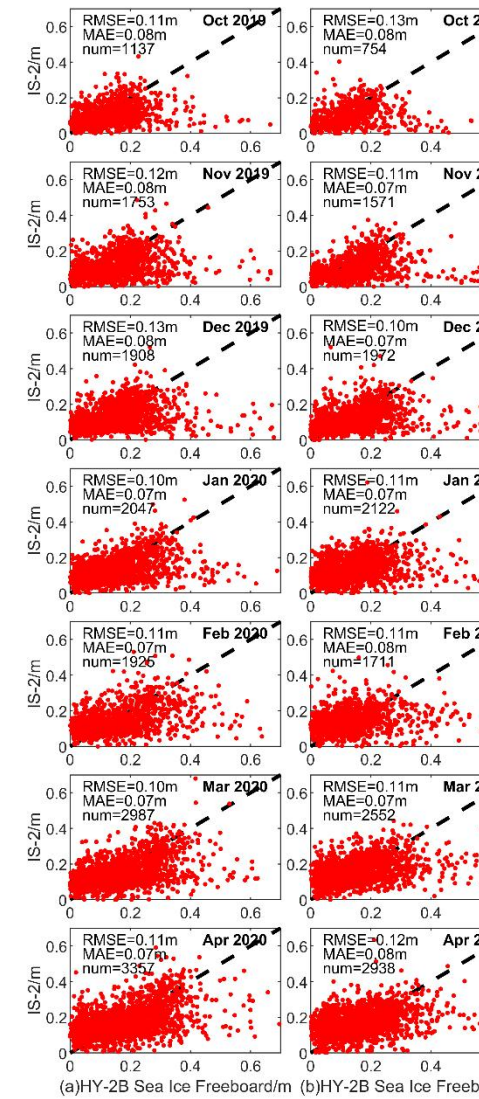
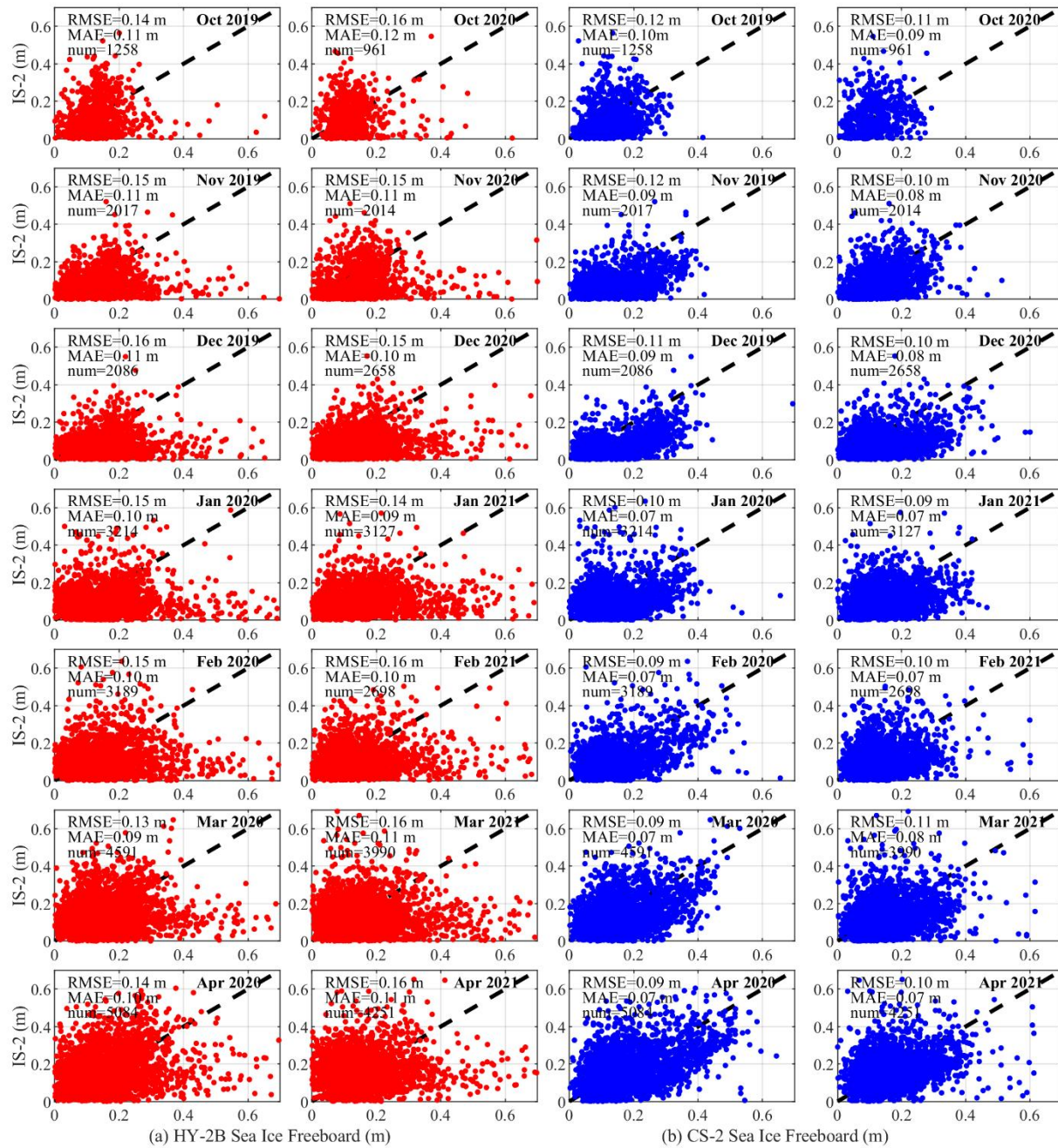
删除[董昭顷]: Comparison between two kinds of sea i ...

725 **Figure 8. Comparative scatter-plots between two satellite products and OIB collected in April 2019: (a) HY-2B sea ice freeboard vs OIB sea ice freeboard, (b) AWI CS-2 sea ice freeboard vs OIB sea ice freeboard, (c) HY-2B sea ice thickness vs OIB sea ice thickness and (d) AWI CS-2 sea ice thickness vs OIB sea ice thickness.**



删除[董昭顷]:

设置格式[董昭顷]: 两端对齐



删除[董昭顷]:

删除[董昭顷]: 12:

删除[董昭顷]: and (c)

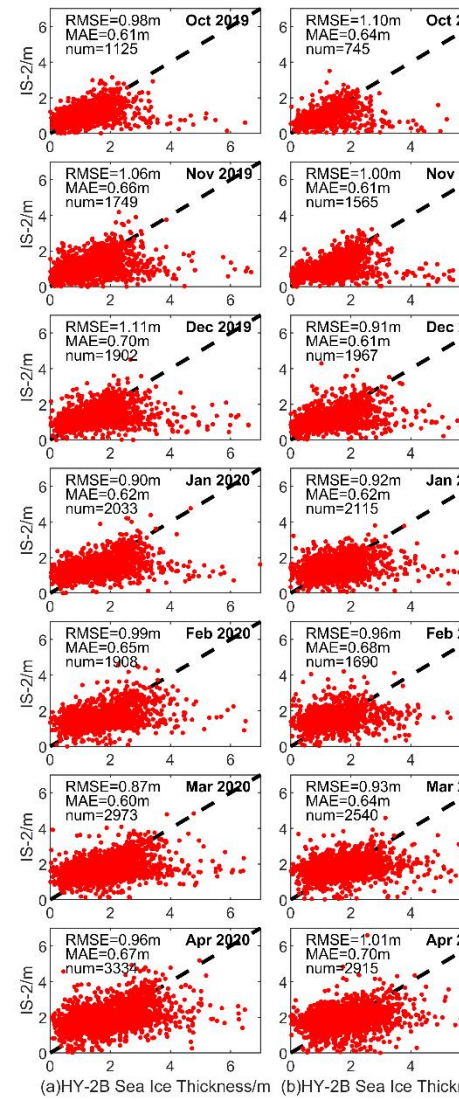
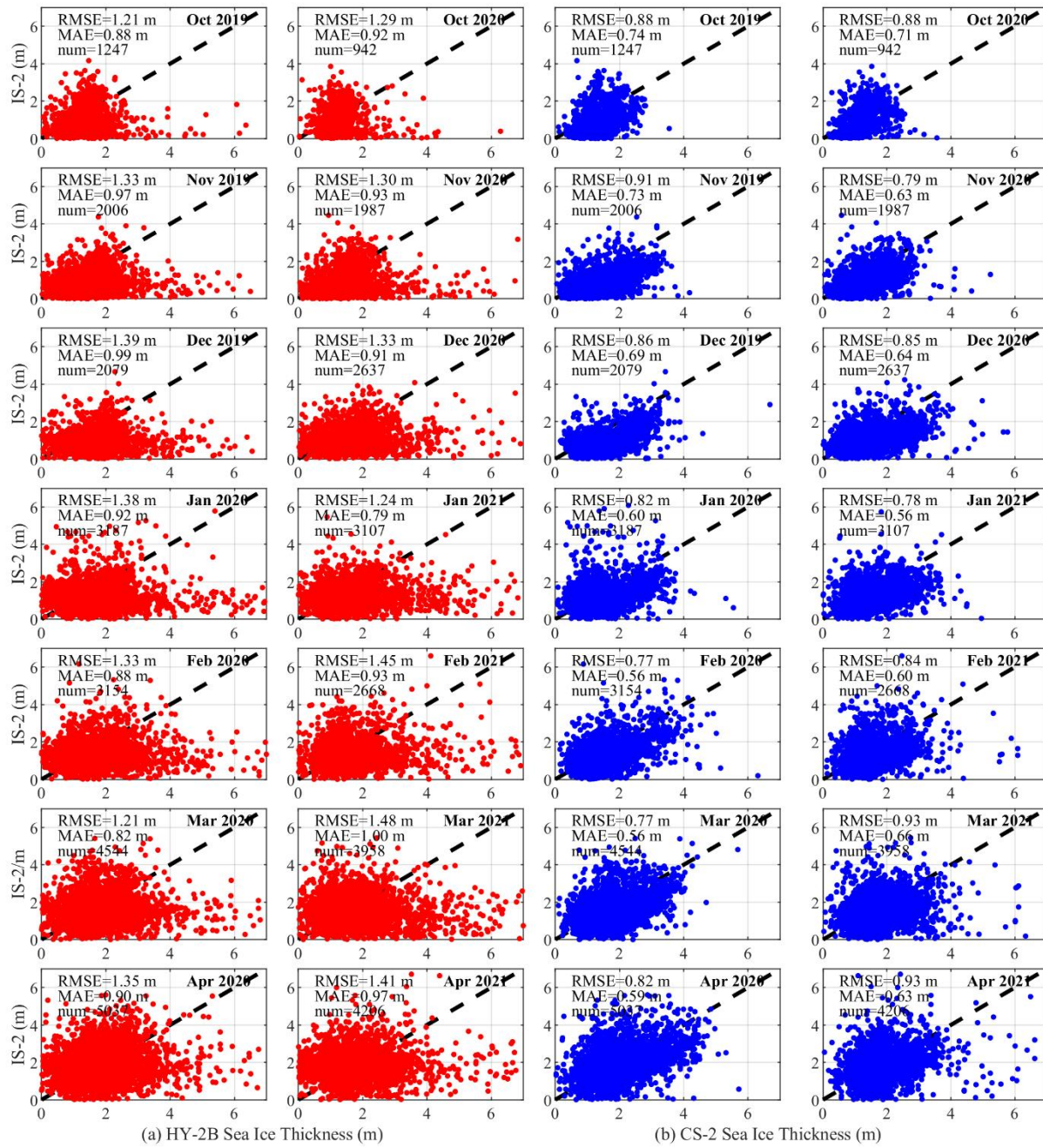
删除[董昭顷]: from October 2019 to April 2020

删除[董昭顷]: and (d)

删除[董昭顷]: comparisons from October 2020 to April 2021

**Figure 9.** Monthly comparisons between HY-2B sea ice freeboard and ICESat-2 sea ice freeboard and between CryoSat-2 sea ice freeboard and ICESat-2 sea ice freeboard values: panels (a) shows comparisons between HY-2B and ICESat-2 in red points, and panels (b) shows comparisons between CS-2 and ICESat-2 in blue points.





删除[董昭顷]:

删除[董昭顷]: 3:

删除[董昭顷]: values

删除[董昭顷]: and (c)

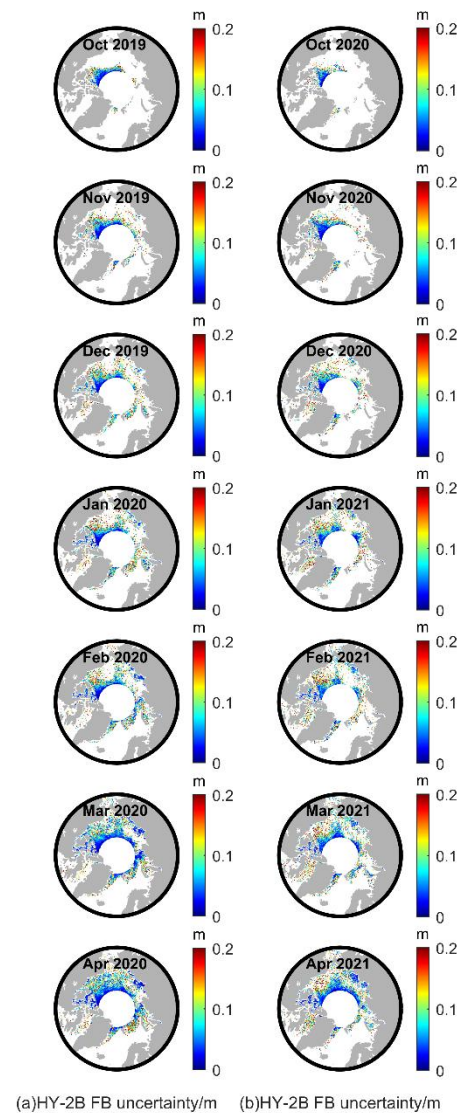
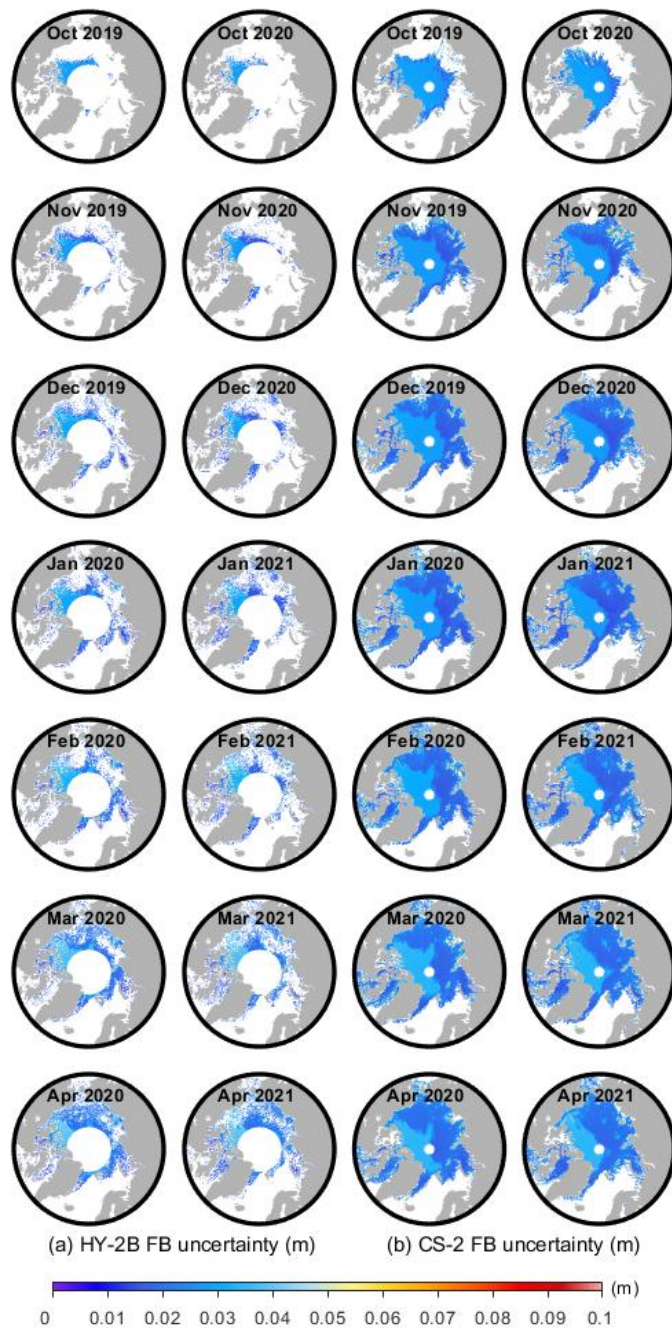
删除[董昭顷]: from October 2019 to April 2020

删除[董昭顷]: and (d)

删除[董昭顷]: from October 2020 to April 2021

**Figure 10.** Monthly comparisons between HY-2B sea ice thickness and ICESat-2 sea ice thickness and between CryoSat-2 sea ice thickness and ICESat-2 sea ice thickness; panels (a) shows comparisons between HY-2B and ICESat-2 in red points, and panels (b) shows comparisons between CS-2 and ICESat-2 in blue points.





删除[董昭顷]:

删除[董昭顷]: 4:

删除[董昭顷]: and (c)

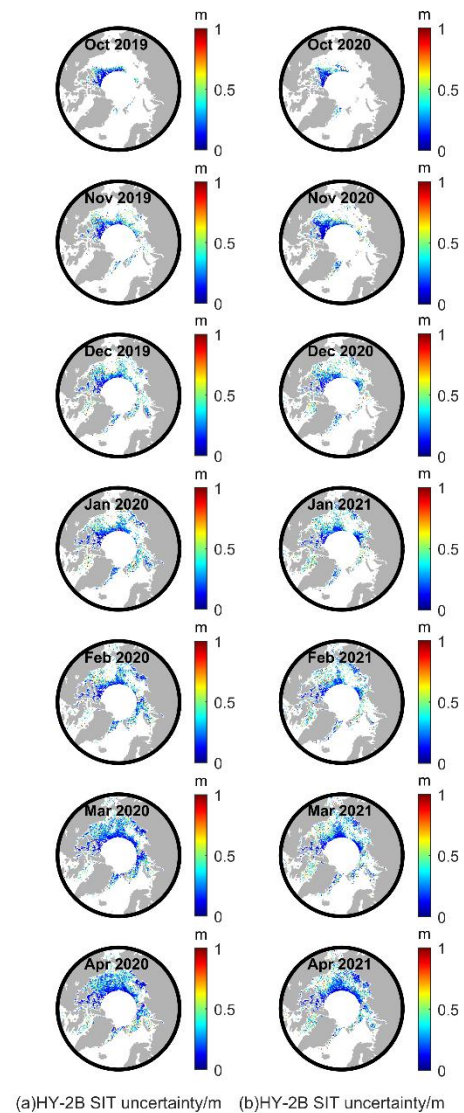
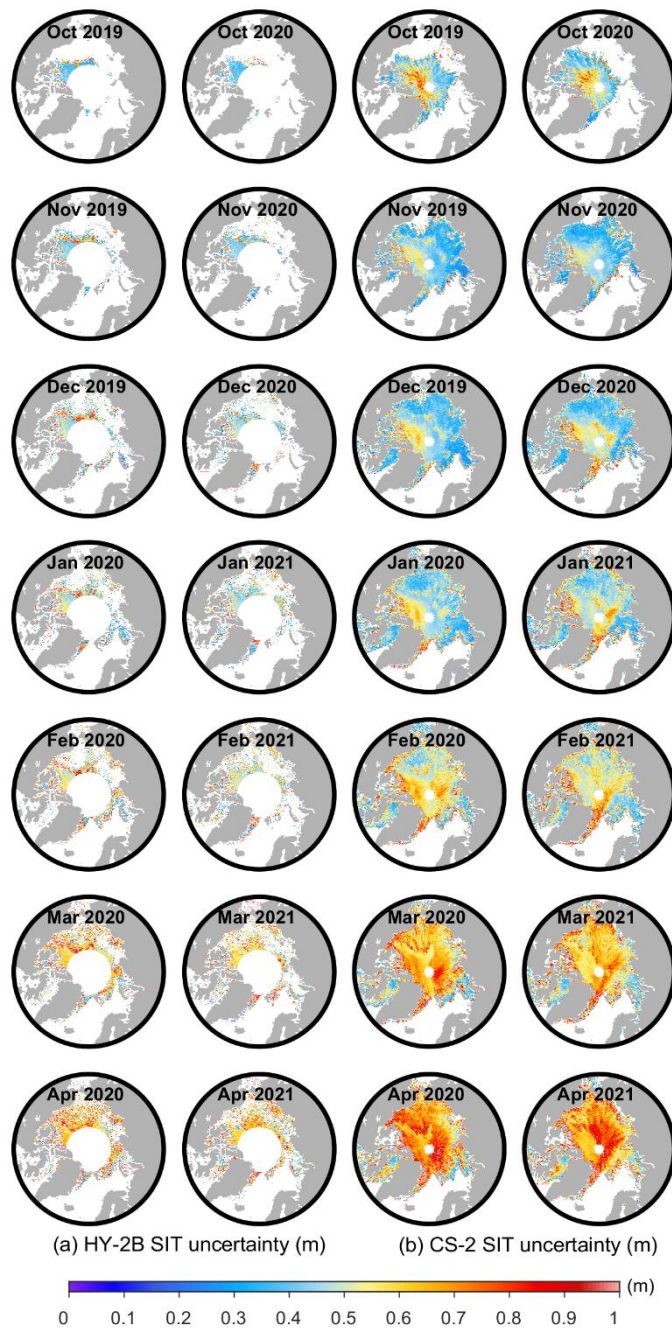
删除[董昭顷]: comparisons from October 2019 to Apr

删除[董昭顷]: and (d)

删除[董昭顷]: comparisons from October 2020 to Apr

740

Figure 1. Monthly comparisons between HY-2B sea ice freeboard uncertainties and CS-2 sea ice freeboard uncertainties from October 2019 to April 2020 and from October 2020 to April 2021: panels (a) shows the HY-2B sea ice freeboard uncertainties, and panels (b) shows the CS-2 sea ice freeboard uncertainties.



删除[董昭顷]:

删除[董昭顷]: 5:

删除[董昭顷]: and (c)

删除[董昭顷]: comparisons from October 2019 to Ap ...

删除[董昭顷]: and (d)

删除[董昭顷]: comparisons from October 2020 to Apr ...

Figure 12. Monthly comparisons between HY-2B sea ice thickness uncertainties and CS-2 sea ice thickness uncertainties from October 2019 to April 2020 and from October 2020 to April 2021: panels (a) shows the HY-2B sea ice thickness uncertainties, and panels (b) shows the CS-2 sea ice thickness uncertainties.



750

**Table 1: HY-2B radar altimeter main parameters.**

Parameter	Value	
Band	Ku	C
Centre frequency	13.58 GHz	5.25 GHz
Chirp signal bandwidth	320/80/20 MHz	160/40/10 MHz
Footprint diameter	1.9 km	10 km
Bandwidth	102.4 us	
Waveform bin number	128	
Range accuracy	< 2 cm	
Spatial coverage	81°N/S	

**Table 2: Comparison of the mean and standard deviation values of the relative surface elevation ( $h_r$ ), sea surface height anomaly (SSHA), and radar freeboard estimates ( $f_r$ ) from HY-2B and CryoSat-2.**

Unit: m	HY-2B		CryoSat-2	
	13 March 2020	4 April 2020	13 March 2020	4 April 2020
$h_r$	0±0.25	0±0.31	0.087±0.25	0.081±0.17
SSHA	-0.11±0.10	-0.21±0.079	-0.069±0.066	-0.051±0.029
$f_r$	0.11±0.27	0.20±0.32	0.16±0.27	0.13±0.18

**Table 3: Mean and modal radar freeboard values of HY-2B and CryoSat-2 over the common area.**

Month	Mean/mode (Unit: m)			
	2019.10-2020.04		2020.10-2021.04	
	HY-2B	CryoSat-2	HY-2B	CryoSat-2
October	0.084/0.066	0.083/0.059	0.085/0.079	0.067/0.051
November	0.087/0.048	0.093/0.074	0.097/0.035	0.077/0.036
December	0.097/0.052	0.081/0.042	0.095/0.064	0.089/0.052
January	0.091/0.049	0.087/0.049	0.096/0.046	0.091/0.049
February	0.097/0.072	0.095/0.061	0.092/0.075	0.098/0.060
March	0.098/0.059	0.110/0.092	0.097/0.048	0.109/0.090
April	0.095/0.072	0.130/0.106	0.090/0.056	0.121/0.102

删除[董昭顷]:

设置格式[董昭顷]: 两端对齐

删除[董昭顷]: Table 2: Time series of snow density va

删除[董昭顷]: 3

删除[董昭顷]: 20

删除[董昭顷]: 18

删除[董昭顷]: 26

删除[董昭顷]: 13

删除[董昭顷]: 24

删除[董昭顷]: 25

删除[董昭顷]: 27

删除[董昭顷]: 23

删除[董昭顷]: 4

删除[董昭顷]: 100

删除[董昭顷]: 118

删除[董昭顷]: 082

删除[董昭顷]: 059

删除[董昭顷]: 096

删除[董昭顷]: 041

删除[董昭顷]: 067

删除[董昭顷]: 051

删除[董昭顷]: 094

删除[董昭顷]: 069

删除[董昭顷]: 089

删除[董昭顷]: 058

删除[董昭顷]: 107

删除[董昭顷]: 117

删除[董昭顷]: 076

755

760



删除[董昭顷]: 5  
删除[董昭顷]: 032  
删除[董昭顷]: 0071  
删除[董昭顷]: 019  
删除[董昭顷]: 068  
删除[董昭顷]: 020  
删除[董昭顷]: 030  
删除[董昭顷]: 012  
删除[董昭顷]: 012  
删除[董昭顷]: 0047  
删除[董昭顷]: 040  
删除[董昭顷]: 023  
删除[董昭顷]: 031  
删除[董昭顷]: 025  
删除[董昭顷]: 0010  
删除[董昭顷]: 018  
删除[董昭顷]: 026  
删除[董昭顷]: 0085  
删除[董昭顷]: 014  
删除[董昭顷]: 0093  
删除[董昭顷]: 013  
删除[董昭顷]: 0094  
删除[董昭顷]: 012  
删除[董昭顷]: 0068  
删除[董昭顷]: 0049  
删除[董昭顷]: 016  
删除[董昭顷]: 0052  
删除[董昭顷]: 012

**Table 4: Differences in the monthly mean radar freeboard values of HY-2B and CryoSat-2 on FYI, MYI and total sea ice.**

Month	2019.10-2020.04			2020.10-2021.04		
	FYI	MYI	ALL	FYI	MYI	ALL
10	0.024	-0.016	0.0015	0.072	0.0031	0.018
11	0.016	-0.053	-0.0061	0.047	-0.011	0.020
12	0.035	-0.035	0.016	0.027	-0.040	0.0056
01	0.016	-0.023	0.041	0.022	-0.032	0.0058
02	0.017	-0.039	0.0022	0.0089	-0.036	-0.0062
03	-0.0024	-0.050	-0.013	-0.0042	-0.036	-0.013
04	-0.022	-0.11	-0.035	-0.023	-0.062	-0.032
mean	0.012	-0.047	0.00094	0.021	-0.031	-0.00026
MAE	0.019	0.047	0.016	0.029	0.031	0.014

**Table 5: Mean and modal sea ice thickness values of HY-2B and CryoSat-2 in the common area.**

Month	Mean/mode (Unit: m)			
	2019.10-2020.04		2020.10-2021.04	
	HY-2B	CryoSat-2	HY-2B	CryoSat-2
October	1.348/0.765	1.337/1.023	1.332/1.280	1.217/1.313
November	1.440/0.892	1.423/1.292	1.504/1.638	1.286/0.551
December	1.583/1.638	1.353/0.891	1.539/1.108	1.445/0.968
January	1.571/1.034	1.475/1.081	1.603/1.095	1.521/1.150
February	1.716/1.261	1.618/1.290	1.637/1.487	1.650/1.189
March	1.752/1.268	1.797/1.794	1.704/1.031	1.790/1.542
April	1.711/1.190	1.970/1.824	1.656/1.328	1.911/1.862

765

770

775

**Table 6: Differences in the monthly mean sea ice thicknesses of HY-2B and CryoSat-2 on FYI, MYI and total sea ice.**

Unit: m	2019.10-2020.04			2020.10-2021.04		
month	FYI	MYI	ALL	FYI	MYI	ALL
October	0.38	-0.21	0.011	0.76	-0.066	0.12
November	0.24	-0.41	0.017	0.48	-0.11	0.22
December	0.42	-0.29	0.23	0.29	-0.35	0.094
January	0.21	-0.22	0.096	0.23	-0.31	0.082
February	0.22	-0.32	0.098	0.11	-0.33	-0.013
March	0.030	-0.42	-0.044	-0.015	-0.35	-0.086
April	-0.17	-0.91	-0.26	-0.20	-0.57	-0.25
mean	0.16	-0.40	0.021	0.24	-0.30	0.024
MAE	0.24	0.40	0.11	0.30	0.30	0.12

- 删除[董 昭顷]: 7
- 删除[董 昭顷]: 456
- 删除[董 昭顷]: 0353
- 删除[董 昭顷]: 155
- 删除[董 昭顷]: 725
- 删除[董 昭顷]: 0575
- 删除[董 昭顷]: 210
- 删除[董 昭顷]: 164
- 删除[董 昭顷]: 137
- 删除[董 昭顷]: 0662
- 删除[董 昭顷]: 414
- 删除[董 昭顷]: 123
- 删除[董 昭顷]: 289
- 删除[董 昭顷]: 221
- 删除[董 昭顷]: 110
- 删除[董 昭顷]: 131
- 删除[董 昭顷]: 260
- 删除[董 昭顷]: 140
- 删除[董 昭顷]: 143
- 删除[董 昭顷]: 115
- 删除[董 昭顷]: 103
- 删除[董 昭顷]: 0589
- 删除[董 昭顷]: 113
- 删除[董 昭顷]: 155
- 删除[董 昭顷]: 390
- 删除[董 昭顷]: 136
- 删除[董 昭顷]: 203
- 删除[董 昭顷]: 5

780

785

790

795

800

**Table 7: Schemes for determining SSHAs.**

Number	Scheme
1	If there are more than 3 observation points per 25-km segment in every track, the average of the 3 lowest values is taken as the SSHA. <u>Otherwise, the SSHA is set to nan and nearest interpolation is performed along track.</u>
2	If there are more than 5 observation points per 25-km segment in every track, the average of the 5 lowest values is taken as the SSHA. <u>Otherwise, the SSHA is set to nan and nearest interpolation is performed along track.</u>
3	If there are more than 7 observation points per 25-km segment in every track, the average of the 7 lowest values is taken as the SSHA. <u>Otherwise, the SSHA is set to nan and nearest interpolation is performed along track.</u>
4	If there are more than 9 observation points per 25-km segment in every track, the average of the 9 lowest values is taken as the SSHA. <u>Otherwise, the SSHA is set to nan and nearest interpolation is performed along track.</u>
5	If there are more than 11 observation points per 25 km segment in every track, the average of the 11 lowest values is taken as the SSHA. <u>Otherwise, the SSHA is set to nan and nearest interpolation is performed along track.</u>
6	If there are more than <u>13</u> observation points per 25-km segment in every track, the <u>average</u> of the <u>13</u> lowest values is taken as the SSHA. <u>Otherwise, the SSHA is set to nan and nearest interpolation is performed along track.</u>
7	If there are more than <u>15</u> observation points per 25-km segment in every track, the <u>average</u> of the <u>15</u> lowest values is taken as the SSHA. <u>Otherwise, the SSHA is set to nan and nearest interpolation is performed along track.</u>
8	If there are more than <u>17</u> observation points per 25-km segment in every track, the <u>average</u> of the <u>17</u> lowest values is taken as the SSHA. <u>Otherwise, the SSHA is set to nan and nearest interpolation is performed along track.</u>

删除[董昭顷]: 8

删除[董昭顷]: Otherwise, the SSHA is set to 0.

删除[董昭顷]: Otherwise, the SSHA is set to 0.

删除[董昭顷]: Otherwise, the SSHA is set to 0.

删除[董昭顷]: Otherwise, the SSHA is set to 0.

删除[董昭顷]: Otherwise, the SSHA is set to 0.

删除[董昭顷]: median

删除[董昭顷]: Otherwise, the SSHA is set to 0.

删除[董昭顷]: median

删除[董昭顷]: Otherwise, the SSHA is set to 0.

删除[董昭顷]: median

删除[董昭顷]: Otherwise, the SSHA is set to 0.

删除[董昭顷]: 9

If there are more than 9 observation points per 25-km segment in every track, the median of the 9 lowest values is taken as the SSHA. Otherwise, the SSHA is set to 0.

10

If there are more than 11 observation points per 25-km segment in every track, the median of the 11 lowest values is taken as the SSHA. Otherwise, the SSHA is set to 0.

设置格式[董昭顷]: 两端对齐

805

810

**Table 8: Table of differences between CryoSat-2 radar freeboard and HY-2B radar freeboard, retrieved by different SSHA determination schemes.**

Unit: m	Oct 2019-Apr 2020			Oct 2020-Apr 2021		
	Mean deviation	MAE	SSHA	Mean deviation	MAE	SSHA
1	0.1524	0.1524	-0.2775	0.1489	0.1489	-0.2696
2	0.0972	0.0972	-0.2235	0.0956	0.0956	-0.2176
3	0.0661	0.0661	-0.1867	0.0670	0.0670	-0.1830
4	0.0410	0.0410	-0.1582	0.0424	0.0424	-0.1556
5	0.0213	0.0244	-0.1357	0.0241	0.0265	-0.1346
6	0.0071	0.0149	-0.1184	0.0102	0.0172	-0.1181
7	-0.0043	0.0111	-0.1042	-0.00008	0.0144	-0.1049
8	-0.0142	0.0162	-0.0923	-0.0089	0.0155	-0.0936

**Table 9: Mean sea ice freeboard uncertainties of HY-2B and CryoSat-2 in the common area.**

Unit: m	Oct 2019-April 2020		Oct 2020-April 2021	
	HY-2B	CS-2	HY-2B	CS-2
October	0.027	0.028	0.025	0.028
November	0.022	0.023	0.022	0.023
December	0.023	0.023	0.022	0.023
January	0.022	0.023	0.021	0.022
February	0.024	0.024	0.023	0.024
March	0.025	0.025	0.025	0.025
April	0.025	0.024	0.025	0.024

**Table 10: Mean sea ice thickness uncertainties of HY-2B and CryoSat-2 in the common area.**

Unit: m	Oct 2019-April 2020		Oct 2020-April 2021	
	HY-2B	CS-2	HY-2B	CS-2
October	0.49	0.49	0.44	0.47
November	0.53	0.46	0.51	0.42
December	0.59	0.46	0.55	0.49
January	0.58	0.50	0.57	0.52
February	0.63	0.56	0.60	0.57
March	0.66	0.63	0.65	0.63
April	0.67	0.69	0.65	0.69

删除[董昭顷]: 9

删除[董昭顷]: values

删除[董昭顷]:

设置格式[董昭顷]: 两端对齐

删除[董昭顷]: 10

删除[董昭顷]: 085

删除[董昭顷]: 014

删除[董昭顷]: 095

删除[董昭顷]: 013

删除[董昭顷]: 10

删除[董昭顷]: 015

删除[董昭顷]: 10

删除[董昭顷]: 014

删除[董昭顷]: 11

删除[董昭顷]: 012

删除[董昭顷]: 11

删除[董昭顷]: 014

删除[董昭顷]: 11

删除[董昭顷]: 013

删除[董昭顷]: 11

删除[董昭顷]: 014

删除[董昭顷]: 10

删除[董昭顷]: 015

删除[董昭顷]: 12

删除[董昭顷]: 015

删除[董昭顷]: 093

删除[董昭顷]: 013

删除[董昭顷]: 11